

UniMMAD: Unified Multi-Modal and Multi-Class Anomaly Detection via MoE-Driven Feature Decompression

Yuan Zhao^{1,2*}, Youwei Pang^{3*}, Lihe Zhang^{1#}, Hanqi Liu²,
Jiaming Zuo^{2#}, Huchuan Lu¹, Xiaoqi Zhao^{3#}

¹IIAU-Lab, Dalian University of Technology, ²X3000 Inspection Co., Ltd, ³AI4X Team, Nanyang Technological University

*equal contribution. #corresponding authors.

Abstract. Existing anomaly detection methods often treat the modality and class as independent factors. Although this paradigm has enriched the development of AD research branches and produced many specialized models, it has also led to fragmented solutions and excessive memory overhead. Moreover, reconstruction-based multi-class approaches typically rely on shared decoding paths, which struggle to handle large variations across domains, resulting in distorted normality boundaries, domain interference, and high false alarm rates. To address these limitations, we propose UniMMAD, a unified framework for multi-modal and multi-class anomaly detection. At the core of UniMMAD is a Mixture-of-Experts (MoE)-driven feature decompression mechanism, which enables adaptive and disentangled reconstruction tailored to specific domains. This process is guided by a “general \rightarrow specific” paradigm. In the encoding stage, multi-modal inputs of varying combinations are compressed into compact, general-purpose features. The encoder incorporates a feature compression module to suppress latent anomalies, encourage cross-modal interaction, and avoid shortcut learning. In the decoding stage, the general features are decompressed into modality-specific and class-specific forms via a sparsely-gated cross MoE, which dynamically selects expert pathways based on input modality and class. To further improve efficiency, we design a grouped dynamic filtering mechanism and an MoE-in-MoE structure, reducing MoE parameter usage by approximately 75% while maintaining sparse activation and fast inference. UniMMAD achieves state-of-the-art performance on 9 anomaly detection datasets, spanning 3 fields, 12 modalities, and 66 classes.

[Code](#)

1 Introduction

Unsupervised anomaly detection (AD), which aims to detect anomalies without relying on abnormal samples, is crucial in practical applications such as manufacturing inspection [1] and medical diagnosis [2]. In real-world scenarios, anomalies appear in diverse forms and often require multiple sensing modalities to be reliably detected. For example, 3D modalities can help identify geometric defects and mitigate the lighting sensitivity risks in RGB images [3].

Existing approaches [3, 5, 8] primarily focus on the fixed modality inputs. They are dedicated to processing a kind of modality combination, as shown in Fig. 1a. However, in real-world scenarios, multiple distinct sensors are typically involved for product quality inspection. As shown in Fig. 1c, infrared cameras are used to detect internal component damage in the “Light” product, while RGB and 3D sensors are essential for identifying color and geometric defects in the “Foam” product.

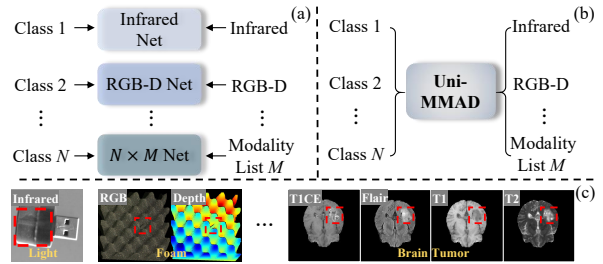


Figure 1. Task setting. (a) Existing methods [3–5] rely on specialized models tailored to the fixed modalities. (b) Our UniMMAD unifies multi-modal and multi-class anomaly detection within a single framework. (c) Visual examples, where anomaly regions, modalities and class names are marked by red boxes, white, and yellow, respectively.

Customizing specific models for each modality combination is not an optimized solution and usually results in difficulties in model deployment and memory overhead. Although existing multi-class methods [6, 9] can be extended to mitigate fragmentation issues with class-shared model designs, they struggle to adapt to complex

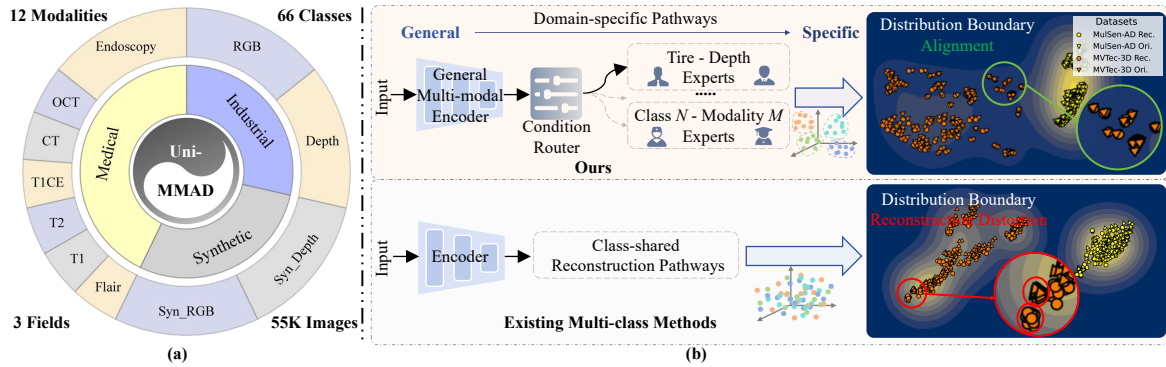


Figure 2. (a) Overview of the fields, modalities, and classes encompassed by UniMMAD. (b) Architectures of UniMMAD and mainstream multi-class methods [6, 7]. Reconstructed feature distribution in normal regions is shown on the right. Larger distances between original features (triangles \blacktriangledown) and reconstructed features (circles \bullet) mean a higher risk of false positives.

modality combinations and diverse scenes, since shared decoders cannot disentangle heterogeneous modality distributions well.

Recently, unified vision models [10–12] have demonstrated that a single architecture and parameter set can handle various tasks. Inspired by these, we aim to develop a unified unsupervised anomaly detection framework across multiple scenarios that supports multi-modal inputs, and predicts multiple semantic classes, as illustrated in Fig. 1b and Fig. 2a. Achieving this goal poses two key challenges: **1) Large domain heterogeneity.** The intricate interplay among diverse modalities and classes introduces large variations in appearance, illumination, scale, background, and anomaly semantics, making consistent representation learning and anomaly discrimination difficult. **2) Practical constraints on efficiency and continual learning.** A practical unified AD model must ensure high accuracy, fast inference, sparse computation, and adapt to new classes or modalities without catastrophic forgetting. Existing multi-class AD models [6, 7] share a reconstruction path across classes. Although parameter-efficient, this shared path aggravates domain interference, resulting in poor normal pattern reconstruction and high false alarms. As shown in Fig. 2b, these methods may distort decision boundaries and misclassify normal regions as anomalies.

To address these challenges, we propose UniMMAD, a unified anomaly detection framework for diverse scenes. Its core is a Mixture-of-Experts (MoE)-based feature decompression mechanism, which is designed to resolve the entanglement caused by heterogeneous inputs. Unified AD requires a shared model to handle large domain shifts across modalities and classes, which often leads to distorted reconstructions and false positives with a single decoder. MoE naturally alleviates this by enabling sparse, input-conditioned expert

activation, letting experts specialize in domains while sharing global parameters. This allows decomposing general latent features into diverse domain-specific outputs. UniMMAD uses a unified encoder to compress arbitrary multi-modal inputs into compact features and a dynamic MoE decoder to adaptively decompress them into task-specific reconstructions with minimal interference.

As shown in Fig. 2b, we first introduce a novel paradigm, “general \rightarrow specific”, which decompresses general multi-modal features into domain-specific unimodal ones. This paradigm encourages the learning of a powerful general-purpose multi-modal encoder that can flexibly adapt to diverse modality combinations and effectively fuse cross-modal information. Unlike conventional reconstruction objectives [6] that reconstruct the input itself, our asymmetric “general \rightarrow specific” paradigm mitigates shortcut reconstruction. Second, we embed a feature compression module in the encoder to generate compact and purified latent representations. This compacts general features and curbs abnormal pattern propagation. Third, in the decoding phase, we design Cross Mixture-of-Experts (C-MoE) to reduce domain interference during decompression. Inspired by the success of MoE on heterogeneous data [13], C-MoE uses a cross-conditioned expert selection mechanism considering general features and domain-specific priors to dynamically choose the optimal decompression pathway. This allows task isolation and adaptive expert scaling. Last, we enhance C-MoE with the grouped dynamic filtering and hierarchical MoE-in-MoE structure. Nesting dense expert groups within sparse MoE and enabling parallel execution can reduce parameter overhead by approximately 75% while preserving the sparse activation benefits of MoE.

Our main contributions can be summarized as follows:

- To the best of our knowledge, we are the first to propose an efficient, unified anomaly detection framework that uses a single set of parameters to handle multi-modal and multi-class data.
- We propose a “general \rightarrow specific” paradigm to learn a general multi-modal encoder and feature compression module for effective cross-modal representation.
- We design the C-MoE, which effectively reduces interference caused by domain gap, while improving the parameter efficiency of MoE.
- UniMMAD shares all parameters and dynamically activates domain-specific experts across diverse scenarios, surpassing state-of-the-art methods with strong continual learning capability and high inference efficiency.

2 Related Work

2.1 Multi-modal Anomaly Detection

Multi-modal anomaly detection integrates complementary information from sensors such as RGB, depth, and surface normals to enhance robustness in complex environments. M3DM [5] uses patch-level contrastive learning and decision-level fusion for RGB and point clouds. MMRD [14] introduces the surface normal modality via reverse distillation. To reduce memory usage, CFM [3] proposes lightweight cross-modal mapping and layer pruning. Different from these methods that train per domain and rely on parameter-free fusion, we propose a “general \rightarrow specific” paradigm with a general encoder, enabling flexible modality combinations and deep cross-modal integration.

2.2 Unified Vision Model

Large-scale foundation models have driven efforts to unify diverse vision tasks with shared parameters. In supervised settings, SegGPT [11] frames segmentation as in-context coloring, and Spider [10] extends this to unify context-independent and medical tasks. For anomaly detection, most methods follow a one-class-one-model scheme. RD [15] uses reverse knowledge distillation, while PatchCore [16] compares memory bank features. UniAD [6] proposes a unified multi-class model within a single-modality dataset. ViTAD [17] and MambaAD [7] further improve performance via transformers and state-space models. To address the challenges of diverse scenes, we propose a practical unified framework that supports anomaly detection across modalities, classes, and fields.

2.3 Mixture-of-Experts

Mixture-of-Experts (MoE) [18] leverages sparsely activated experts for scalable conditional computation. Sparsely-Gated MoE [19] activates a subset of experts per input, while SoftMoE [20] improves stability via differentiable routing. DeepSeekMoE [21] enhances parameter efficiency through shared experts. In vision tasks, V-MoE [22] embeds MoE layers into ViTs. Recent works [23, 24] adopt self-routing MoE structures for anomaly detection, where inputs act as both router and expert targets, leading to limited condition awareness. In this work, we propose C-MoE with a cross-condition router to enhance condition awareness by explicitly disentangling modality and class interference.

3 Method

The overall architecture is shown in Fig. 3. In this section, we first introduce the main idea of the “general \rightarrow specific” paradigm. Next, we describe the general multi-modal encoder for compressing multi-modal features and the Cross Mixture-of-Experts (C-MoE) for decompressing those features into domain-specific ones. Finally, we outline the training and inference processes.

3.1 General \rightarrow Specific

To handle diverse modality combinations and domain discrepancies, we propose a “general \rightarrow specific” paradigm. Its core idea is to decompress multi-modal features into multiple uni-modal ones: $f^{\text{gen}} \rightarrow \{u^m\}_{m=1}^M$, where f^{gen} is the multi-modal feature, u^m is the m -th uni-modal feature, and M is the number of modalities. The model learns this decomposition on normal samples by predicting the residual between f^{gen} and each u^m . A pre-trained prior generator provides domain-specific priors to guide and supervise the decompression process, helping the model capture both general and modality-specific features. During inference, this decompression fails on anomalies, and the resulting deviations serve as indicators for anomaly detection.

3.2 General Multi-modal Encoder

As shown in Fig. 3, the general multi-modal encoder includes an input embedding layer, residual blocks, and a Feature Compression Module (FCM). The input embedding layer pads all inputs to a unified channel dimension C , supporting arbitrary modality combinations: $\mathbb{R}^{C_{\text{in}} \times H \times W} \rightarrow \mathbb{R}^{C \times H \times W}$. Three residual blocks are used to progressively extract multi-modal features, combined with inter-modal prior averages to refine the

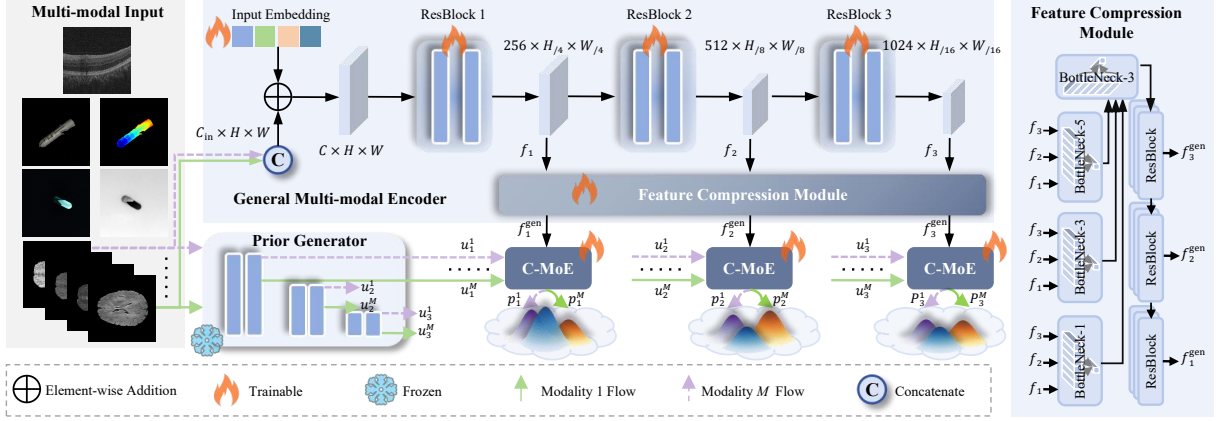


Figure 3. Overview of the UniMMAD. It processes various modality combinations via a general multi-modal encoder and a Feature Compression Module (FCM). The FCM comprises a hierarchical Bottleneck- K structure and residual blocks (ResBlock), where Bottleneck- K uses $K \times K$ convolutions to capture scale information and 1×1 convolutions to adjust dimensions. A prior generator provides domain-specific priors to guide the C-MoE in decompressing general features into domain-specific ones.

features. To prevent anomaly cues from contaminating multi-modal features, FCM employs a hierarchical bottleneck. An inner multi-scale bottleneck uses parallel 1×1 , 3×3 , and 5×5 convolutions to preserve normal patterns while suppressing scale-sensitive anomalies. An outer bottleneck performs finer compression at higher semantic levels to further remove residual abnormal activations. Finally, residual blocks restore the compressed features to multi-scale outputs f_1^{gen} , f_2^{gen} , and f_3^{gen} , yielding purified general features.

3.3 Cross Mixture-of-Experts

C-MoE decompresses general features f_l^{gen} into domain-specific features p_l^m , guided by domain priors u_l^m that encode multi-scale domain knowledge, with l representing the index of feature maps. Instead of relying on cross attention, which may cause shortcut issues [6] and high computational overhead, C-MoE adopts a cross-condition routing strategy. It selects implicit experts based on the priors, enhancing condition awareness and reducing interference across modalities and classes. This mechanism serves as the basis for the following routing and expert design modules.

Condition Router. As shown in Fig. 4, general features are projected to keys and values, and priors to queries. A convolutional layer followed by global average pooling yields global statistics g_l^m , which encapsulate domain-specific contextual characteristics and effectively suppress anomalous leakage, thereby preventing shortcut learning. A gating function G produces top- K expert indices \mathcal{I} and logits, further normalized by softmax to obtain cross-condition scores. To encourage balanced expert usage, we introduce an annealed

load-balancing loss:

$$\mathcal{L}_{\text{MoE}} = \frac{1}{ML} \sum_{m=1}^M \sum_{l=1}^L (1 - \frac{e}{E})^2 \cdot CV(G(g_l^m)), \quad (1)$$

where e , E , and L represent the epoch index, total number of epochs, and the number of feature maps, respectively. The Coefficient of Variation $CV(\cdot)$ quantifies the uniformity of the gate's output distribution. This scheme encourages broad expert activation early and stabilizes routing later.

Expert Design and Routing. C-MoE employs two types of experts: (1) a fixed expert to capture shared knowledge and reduce redundancy, and (2) routed experts selected via top- K gating to provide task-specific capabilities. To reduce memory cost and avoid inactive experts, we construct a MoE-in-MoE structure. Each routed expert (MoE-Leader) is a weighted composition of shared base experts $W \in \mathbb{R}^{N_{\text{exp}} \times O \times I \times K_s \times K_s}$, where N_{exp} is the number of base experts, O and I represent output and input channels, respectively, and K_s is the kernel size. Each MoE-Leader stores only weights $S \in \mathbb{R}^{N_{\text{exp}} \times O}$ for selecting base experts. Given routing indices \mathcal{I} , final convolution kernels are computed as:

$$\hat{W} = \sum_{i \in \mathcal{I}} S'[i, o] \cdot W[i, o], \quad \text{for each } o \in [1, O], \quad (2)$$

where S' is softmax-normalized S along the first dimension. This design enables efficient reuse of base experts, diverse MoE-Leader construction, and better parameter efficiency.

Inference Acceleration and Multi-scale Aggregation. To accelerate C-MoE inference, we introduce two optimizations. (1) *Pre-computed kernels.* Dur-

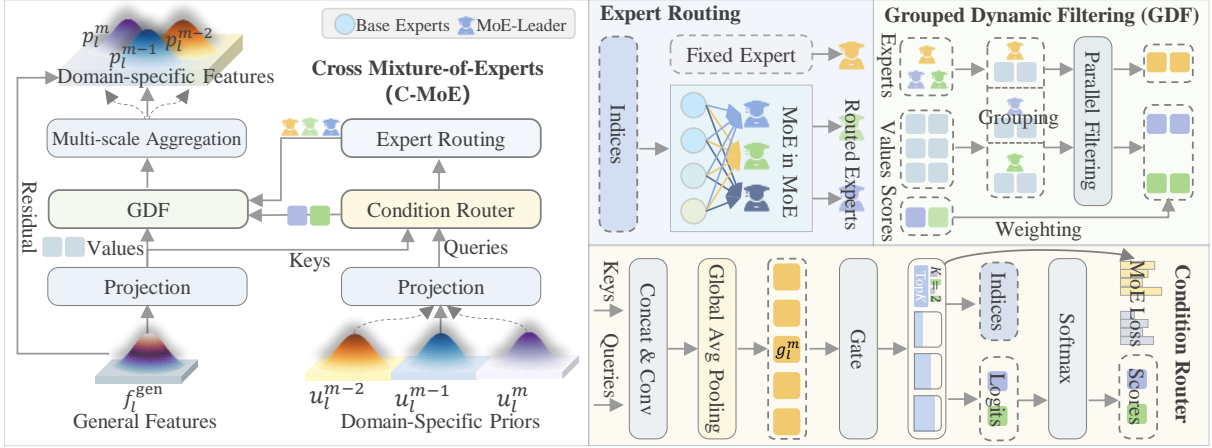


Figure 4. Detailed architecture of C-MoE. It selects expert indices based on domain-specific priors using a condition router, activates the corresponding routed experts and a fixed expert, and decompresses general features via grouped dynamic filtering. Each routed expert adopts an MoE-in-MoE structure to improve parameter efficiency.

ing inference, MoE-in-MoE caches the pre-weighted convolution kernels \hat{W} , eliminating on-the-fly kernel generation. (2) *Grouped dynamic filtering*. The values are replicated for the K_{route} activated routed experts and one fixed expert, and reshaped from $[B = (K_{\text{route}} + 1), C_{\text{val}}, \dots]$ to $[B = 1, (K_{\text{route}} + 1) \times C_{\text{val}}, \dots]$, where C_{val} denotes the channel dimension of values. Setting groups = $K_{\text{route}} + 1$ executes the expert filters within a single group convolution, enabling parallel dynamic filtering and reducing memory traffic and latency by eliminating serial passes. The filtered outputs are weighted and aggregated according to the expert scores produced by the router. To cope with objects of different spatial extents, C-MoE further employs experts with heterogeneous receptive fields and fuses their outputs through an aggregation convolution.

3.4 Training and Inference

Training. We adopt a weighted sampling strategy to balance the different training tasks, where each task’s sampling probability is inversely proportional to the number of samples per class. We introduce a decompression consistency loss \mathcal{L}_{Dec} to enforce alignment between decompressed uni-modal features and their original counterparts, as defined below:

$$\mathcal{L}_{\text{Dec}} = \frac{1}{ML} \sum_{m=1}^M \sum_{l=1}^L \sum_{h=1}^{H_l} \sum_{w=1}^{W_l} \frac{1}{H_l W_l} \text{sg}(A_l^m)^\gamma \odot A_l^m, \quad (3)$$

$$A_l^m(h, w) = 1 - \frac{u_l^m(h, w)^T \cdot p_l^m(h, w)}{\|u_l^m(h, w)\| \cdot \|p_l^m(h, w)\|},$$

where \odot denotes element-wise multiplication, and H_l and W_l denote the height and width of the l -th feature map. For the m -th modality at coordinate (h, w) in

layer l , the anomaly map A_l^m is defined as the negative cosine similarity between the domain-specific prior u_l^m and the corresponding feature p_l^m from the C-MoE. The loss incorporates a focal loss [29]-like modulation factor γ to place greater emphasis on minority classes, where $\text{sg}(\cdot)$ denotes the stop-gradient operation. The overall objective is end-to-end optimized by $\mathcal{L} = \mathcal{L}_{\text{Dec}} + \mathcal{L}_{\text{MoE}}$.

Inference. The model uses the discrepancy between the decompressed uni-modal features and their original counterparts to localize anomalies, as follows:

$$\mathcal{S}_{\text{AL}} = \frac{1}{L} \sum_{l=1}^L \Phi \left(\sqrt{\sum_{m=1}^M (A_l^m)^2} \right), \quad (4)$$

where $\Phi(\cdot)$ upsamples the anomaly map to the input size and smooths it using a Gaussian kernel with $\sigma = 4$, as in [3]. The image-level anomaly detection score \mathcal{S}_{AD} is computed as the average of the top 0.1% of anomaly localization scores.

4 Experiments

4.1 Datasets and Evaluation Metrics

We conduct experiments on 9 widely used AD datasets, with Hyper-Kvasir [30], Retinal OCT [31], and Liver CT [32] unified into the UniMed dataset. Detailed dataset information is summarized in the Appendix (Tab. 8). We follow the training settings of recent state-of-the-art methods in these tasks and merge all training samples together as our training set. We adopt both image-level and pixel-level metrics to evaluate all the models. For the image-level metrics, we report the Area Under the Receiver Operating Characteristic Curve (AUC_I), Average Precision (AP_I), and the maxi-

Table 1. Quantitative comparison at the image level across multi-scene datasets, with the best in **bold** and second-best underlined.

Methods	Publications	MVTec-3D		Eyecandies		MulSen-AD		BraTs		UniMed	
		AUC _I	MF1 _I								
Specialized Models (One model for one dataset)											
M3DM [5]	CVPR2023	92.129	94.134	77.387	76.039	-	-	-	-	-	-
CFM [3]	CVPR2024	<u>92.443</u>	<u>93.731</u>	<u>81.847</u>	<u>79.668</u>	-	-	-	-	-	-
MulSen-TripleAD [4]	CVPR2025	-	-	-	-	<u>78.867</u>	92.832	-	-	-	-
PatchCore+MMRD	-	-	-	-	-	-	-	<u>91.827</u>	<u>90.471</u>	-	-
UniAD [6]	NeurIPS2022	-	-	-	-	-	-	-	-	90.847	90.934
RD [15]	CVPR2022	-	-	-	-	-	-	-	-	93.432	91.581
ViTAD [17]	CVIU2025	-	-	-	-	-	-	-	-	95.524	93.648
MambaAD [7]	NeurIPS2024	-	-	-	-	-	-	-	-	95.977	93.678
SimpleNet [25]	CVPR2023	-	-	-	-	-	-	-	-	89.422	88.515
INP-Former [9]	CVPR2025	-	-	-	-	-	-	-	-	<u>96.060</u>	94.363
Generalist Models (One model performs all AD tasks without fine-tuning)											
AdaCLIP [26]	ECCV2024	74.134	89.929	73.134	74.809	59.127	78.126	70.674	81.603	83.845	91.247
MVEA [27]	CVPR2024	62.781	89.474	64.817	70.268	65.781	79.973	63.749	79.934	88.138	87.219
AA-CLIP [28]	CVPR2025	71.827	90.436	48.137	65.642	77.847	<u>92.261</u>	57.647	80.174	72.253	84.193
Unified Multi-modal and Multi-class Model											
Ours	-	92.527	94.903	85.566	84.103	85.460	90.236	95.838	91.139	96.335	<u>94.182</u>

imum F1 score (MF1_I), following the methodology in the literature [33, 34]. For the pixel-level metric, we report the Area Under the Receiver Operating Characteristic Curve (AUC_P), Area Under the Per-Region-Overlap (AUPRO) and the maximum F1 score (MF1_P). MF1_I and MF1_P are critical metrics for evaluating anomaly detection and localization performance [35], representing the upper bounds of performance at the image and pixel levels, respectively.

4.2 Implementation Details

Following common practice [14, 16] in anomaly detection, we adopt WideResNet50 [36] as the prior generator to extract the first three layers as domain-specific priors. All images are resized to 256×256 to ensure fair comparisons. We train and test specialized methods on their respective tasks in a conventional multi-class setting with a consistent backbone and experimental setup, while evaluating generalist methods across all datasets by predicting each modality independently and aggregating the results. In C-MoE, we employ 8 shared base experts and 32 MoE-Leaders, while the multi-scale experts use 1×1 , 3×3 , and 5×5 kernels. The K for the activated top- K routed experts is set to 2. The decompression consistency loss uses $\gamma = 2$, following focal loss [29]. Additional experimental details, comparison methods and dataset descriptions can be found in the Appendix.

4.3 Quantitative Results

The image-level and pixel-level results are shown in Tab. 1 and Tab. 2, respectively. Although trained only

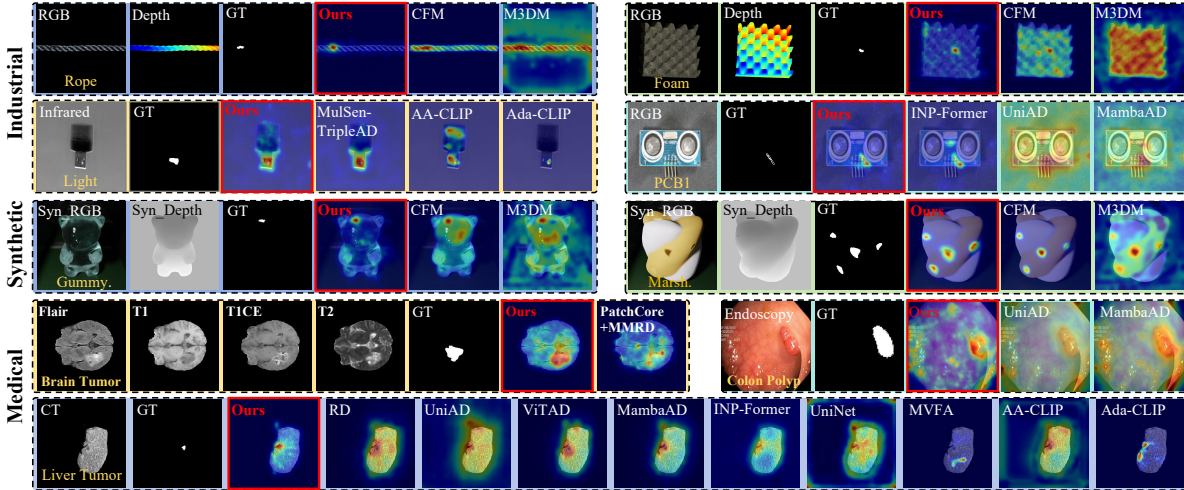
once on the entire dataset, UniMMAD consistently outperforms most specialized methods. It surpasses strong multi-modal baselines on MVTec-3D and BraTs, and improves pixel-level MF1_P by 7.5% on Eyecandies. On uni-modal tasks, generalist models transfer well to UniMed but still underperform compared with existing multi-class methods. Furthermore, the proposed method is compared with mainstream multi-class methods on the traditional industrial datasets MVTec-AD and VisA under the super-multi-class setting [9], which constructs a unified model for industrial scenarios. As shown in Tab. 3, the proposed method outperforms current approaches, particularly in the complex multi-instance scenes of VisA, achieving a 10.8% improvement in MF1_P than INP-Former [9]. These results show that UniMMAD generalizes well across diverse AD tasks, while maintaining high accuracy without per-task customization.

4.4 Qualitative Results

We show some qualitative comparisons in Fig. 5. Compared to specialist methods, UniMMAD generates more precise and sharper activations on defect regions while maintaining minimal responses in normal areas. Examples include detail-rich ‘‘Rope’’, boundary-blurred ‘‘Brain Tumor’’, and low-contrast ‘‘Light’’. Although generalist models can produce concentrated activation maps, they often highlight normal or benign regions resulting in false positives. Additional qualitative discussions are provided in the Appendix.

Table 2. Quantitative comparison at the pixel level across multi-scene datasets, with the best in **bold** and second-best underlined.

Methods	Publications	MVTec-3D		Eyecandies		MulSen-AD		BraTs		UniMed	
		AUC _P	MF1 _P								
Specialized Models (One model for one dataset)											
M3DM [5]	CVPR2023	98.914	44.721	93.758	36.527	-	-	-	-	-	-
CFM [3]	CVPR2024	98.757	44.137	<u>95.838</u>	31.916	-	-	-	-	-	-
MulSen-TripleAD [4]	CVPR2025	-	-	-	-	97.833	<u>33.640</u>	-	-	-	-
PatchCore+MMRD	-	-	-	-	-	-	-	95.717	46.737	-	-
UniAD [6]	NeurIPS2022	-	-	-	-	-	-	-	-	87.020	39.435
RD [15]	CVPR2022	-	-	-	-	-	-	-	-	90.514	40.012
ViTAD [17]	CVIU2025	-	-	-	-	-	-	-	-	91.828	44.441
MambaAD [7]	NeurIPS2024	-	-	-	-	-	-	-	-	91.687	42.401
SimpleNet [25]	CVPR2023	-	-	-	-	-	-	-	-	86.858	39.136
INP-Former [9]	CVPR2025	-	-	-	-	-	-	-	-	92.670	45.477
Generalist Models (One model performs all AD tasks without fine-tuning)											
AdaCLIP [26]	ECCV2024	96.924	37.106	95.173	32.047	<u>97.835</u>	29.752	<u>96.553</u>	<u>48.439</u>	90.729	42.852
MVFA [27]	CVPR2024	93.264	14.012	82.650	11.105	90.381	15.817	94.348	33.426	87.514	34.281
AA-CLIP [28]	CVPR2025	98.025	42.141	94.744	27.205	97.531	32.501	94.964	29.991	90.943	40.325
Unified Multi-modal and Multi-class Model											
Ours	-	99.089	<u>44.159</u>	96.913	39.436	97.919	34.666	97.468	51.404	<u>92.015</u>	<u>44.893</u>

**Figure 5.** Qualitative comparisons across three fields, with our method highlighted in red, modality in white and class in yellow.**Table 3.** Quantitative comparison on the MVTec-AD and VisA datasets under the super-multi-class setting with a resolution of 256×256 , evaluated using image-level metrics (AUC_I/AP_I/MF1_I) and pixel-level metrics (AUC_P/MF1_P/AUPRO).

Datasets	MVTec-AD		VisA	
	Image-level	Pixel-level	Image-level	Pixel-level
RD [15]	95.8/97.8/95.0	95.1/51.5/90.7	88.4/89.9/86.7	96.8/38.7/87.0
UniAD [6]	95.0/97.7/94.5	95.8/46.8/90.0	90.7/92.2/86.9	98.3/38.1/88.8
ViTAD [17]	97.7/98.9/96.5	97.1/57.0/90.9	89.1/90.4/85.4	98.0/39.8/84.2
MambaAD [7]	94.7/97.7/94.5	96.3/51.5/90.5	90.2/91.4/87.5	97.7/39.4/87.9
INP-Former [9]	99.2/99.5/98.6	98.2/60.7/93.8	95.2/95.7/91.9	98.8/44.4/91.5
Ours	99.4/99.6/98.7	98.1/60.2/93.0	95.5/96.2/92.4	98.9/47.2/91.3

4.5 Ablation Studies

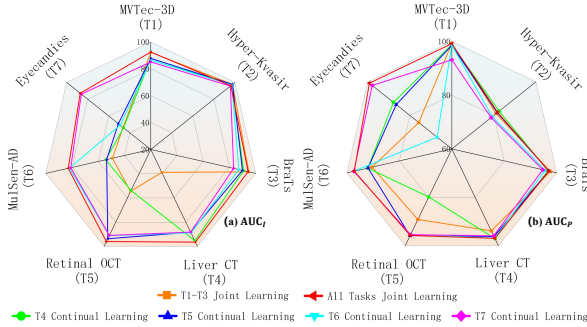
We adopt the Reverse Teacher-Student framework [15] as our baseline due to its clear architecture and reliable performance, which makes it a strong foundation for extension to our unified setting. However, the original

design is limited to single-modality input. To adapt this baseline to various modality combinations, we use a pre-trained model to extract uni-modal features and then fuse them into multi-modal representations using the parameter-free modulation from MMRD [14]. These modifications allow the baseline to support the unified detection task and provide a fair baseline for evaluating the effectiveness of each design in UniMMAD. Tab. 4 presents detailed ablation results in terms of both image-level and pixel-level metrics.

Architecture. First, we replace the OCBE module [15] with FCM and achieve significant improvements on UniMed datasets. This is because FCM compresses normal features and enlarges their separation from anomalies, making the model more sensitive to subtle defects. Next, we adopt a “general \rightarrow specific” paradigm. A gen-

Table 4. Overall ablation study on the architecture, C-MoE, and training strategies.

Methods	Mean			MVTec-3D			Eyecandies			MulSen-AD			BraTs			UniMed		
	AUC _I	AUC _P	MF1 _P	AUC _I	AUC _P	MF1 _P	AUC _I	AUC _P	MF1 _P	AUC _I	AUC _P	MF1 _P	AUC _I	AUC _P	MF1 _P	AUC _I	AUC _P	MF1 _P
(a) Architecture																		
Baseline	75.624	86.616	28.464	82.760	98.867	39.287	58.151	53.832	10.691	79.913	98.006	34.099	69.253	91.873	19.720	88.044	90.501	38.524
+ FCM	77.367	86.651	28.926	84.316	98.940	39.160	57.069	52.497	9.687	80.747	98.187	33.453	73.226	92.643	21.625	91.478	90.987	40.705
+ General→Specific	84.306	96.105	37.132	89.670	99.080	44.983	67.920	96.580	27.491	80.360	97.860	31.215	90.747	95.628	39.706	92.832	91.376	42.266
+ C-MoE	91.145	96.681	42.912	92.527	99.089	44.159	85.566	96.913	39.436	85.460	97.919	34.666	95.838	97.468	51.404	96.335	92.015	44.893
(b) C-MoE																		
w/o Cross-condition	85.126	95.682	37.918	88.394	98.394	40.906	80.859	95.622	38.347	80.805	97.817	31.713	86.575	94.849	35.650	88.997	91.668	42.974
w/o Multi-scale Exp.	88.900	96.430	41.218	92.922	99.276	44.784	85.739	97.040	40.100	81.960	97.779	31.124	91.311	96.478	46.438	92.572	91.577	43.646
w/o Routed Experts	85.417	95.967	37.822	88.275	98.431	41.369	80.000	95.646	37.040	79.750	97.645	30.014	88.010	94.594	33.583	91.051	91.875	43.355
w/o Fixed Expert	89.424	96.475	41.482	91.751	99.244	44.585	86.233	97.228	40.901	82.823	97.463	31.687	92.602	96.874	49.566	93.713	91.567	40.673
Ours	91.145	96.681	42.912	92.527	99.089	44.159	85.566	96.913	39.436	85.460	97.919	34.666	95.838	97.468	51.404	96.335	92.015	44.893

**Figure 6.** Image- / pixel-level performance of UniMMAD in continual learning on new tasks. UniMMAD is initially trained jointly on tasks T1–T3, then incrementally fine-tuned on tasks T4–T7. It achieves performance comparable to training all tasks jointly.

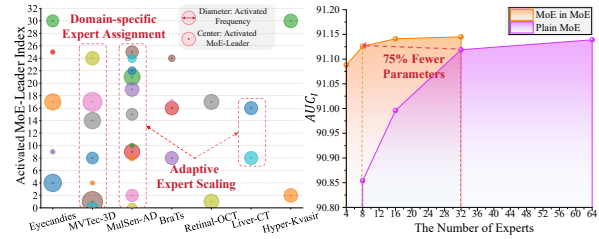
eral encoder extracts multi-modal features, which are decompressed via cross attention. This design captures shared cues while restoring modality-specific details. It yields 8.9% and 10.9% gains in AUC_I and AUC_P, respectively. Finally, we integrate the proposed C-MoE and improve AUC_I by an average of 8.1% across the industrial, synthetic, and medical fields. In summary, Tab. 4 validates the effectiveness of each component without exception.

C-MoE. The core designs of C-MoE are cross-condition mechanisms and routed experts. Replacing the cross-condition MoE with a plain MoE leads to an average drop of 6.7% in terms of AUC_I. Removing routed experts implicitly disables the cross-condition mechanism, leading to a 5.7% drop in AUC_I. Besides, both multi-scale and fixed experts contribute to further performance improvements. We can see that multi-scale experts help capture large tissue anomalies and small tumors, improving AUC_I by 4.6% on UniMed.

Continual Learning. Fig. 6 shows the continual learning ability of UniMMAD. First, we jointly train tasks T1–T3 to obtain a basic general detection capability. Then, we progressively conduct the continual learning from T4 to T7, where we only fine-tune less than 10% parameters from the MoE-leader, condition router,

Table 5. Comparison (AUC_I/AUC_P/MF1_P) with Gains (Δ) between Specialized (Speci.) and Unified Training for our UniMMAD and Baseline.

Methods	Mean	MVTec-3D	Eyecandies	MulSen-AD	BraTs	UniMed
Baseline/Speci.	81.2/89.9/33.0	87.2/99.1/42.4	61.4/65.5/11.0	77.8/98.1/32.8	88.3/96.0/36.0	91.6/90.8/43.1
Baseline/Unified	75.6/86.6/28.4	82.7/98.8/39.2	58.1/53.8/10.6	79.9/98.0/34.0	69.2/91.8/17.7	88.0/90.5/38.5
Δ Speci.-Unified	5.6/3.3/4.6	4.5/0.3/3.2	3.3/11.7/0.4	7.2/0.1/1.2	19.1/4.2/16.3	3.6/0.3/4.6
Ours/Speci.	91.2/96.7/43.2	92.9/99.1/45.6	86.7/97.1/40.8	83.4/97.5/34.3	95.0/97.2/49.9	97.7/92.6/45.5
Ours/Unified	91.1/96.6/42.9	92.5/99.0/44.1	85.5/96.9/39.4	85.4/97.9/34.6	95.8/97.4/51.4	96.3/92.0/44.8
Δ Speci.-Unified	0.1/0.1/0.3	0.4/0.1/1.5	1.2/0.2/1.4	2.0/0.4/0.3	0.8/0.2/1.5	1.4/0.6/0.7

**Figure 7.** (a) Left: Activation frequency of each MoE-leader across different datasets, illustrating domain-specific expert selection. (b) Right: Comparison of parameter efficiency between MoE-in-MoE and plain MoE for performance for different numbers of experts.

and aggregation convolution. To retain routing accuracy for early tasks, 1% of the previous data is mixed in during the training of each new task. Finally, UniMMAD achieves comparable performance on new tasks to joint training on all tasks, while the performance degradation on previous tasks is less than 8%.

Task isolation within MoE. Fig. 7(a) shows that C-MoE assigns distinct experts to different domains, mitigating interference across modalities and classes. C-MoE also dynamically adjusts the number of selected experts to match dataset complexity. For example, MulSen-AD exhibits high intra-class variability, while MVTec-3D introduces even more complex modality variations, thereby requiring more experts. Compared to fixed reconstruction pathways, C-MoE offers greater flexibility and scalability.

MoE in MoE. To evaluate parameter efficiency, we compared MoE-in-MoE with plain MoE under different expert configurations. The number of MoE-in-MoE experts is fixed at 32. The number of base experts serving as the primary source of parameters is variable. Fig. 7 (b) shows that MoE-in-MoE achieves performance com-

Table 6. Efficiency comparison on NVIDIA 4090. “-” represents memory bank-based methods without parameters(Param.), activated parameters(ActPar.) and FLOPs.

Methods	FPS (fps)↑	Memory (M)↓	Param. (MB)↓	ActPar. (MB)↓	FLOPs (GFlops)↓
M3DM [5]	0.39	73774.53	-	-	-
MulSen. [4]	1.19	10323.05	-	-	-
CFM [3]	13.18	3757.12	113.17	113.17	431.14
Ours	59.09	4970.17	233.66	192.38	110.91

parable to the plain MoE while using 75% fewer parameters. With the increasing number of parameters, the performance gains of MoE-in-MoE gradually saturate.

Unified vs. Specialized. Unlike baselines suffering from parameter interference, UniMMAD maintains exceptional stability (Tab. 5) by effectively disentangling domain conflicts via adaptive routing. Additionally, unified training yields the gains on data-scarce infrared modalities (MulSen-AD) and complex 4-modality BraTs.

Efficiency. As shown in Tab. 6, the proposed model integrates multi-field, multi-modal, and multi-class data with a parameter count comparable to specialized multi-modal methods. Memory bank-based methods such as M3DM and MulSen-TripleAD (MulSen.) show slower inference and high memory overhead, while CFM also suffers from inefficiency due to the heavy Transformer architecture and point cloud processing. In contrast, our fully convolutional MoE-in-MoE design reuses base experts, yielding faster inference, making it well suited for practical anomaly detection.

5 Conclusion

We introduce UniMMAD, a unified model designed for multi-modal and multi-class anomaly detection. It incorporates a “general \rightarrow specific” paradigm, a general multi-modal encoder, and a parameter-efficient C-MoE. Extensive experiments on nine challenging benchmarks demonstrate that UniMMAD establishes a new state-of-the-art, outperforming specialized methods using only a single set of parameters. Furthermore, UniMMAD provides a strong baseline for unified multi-scene anomaly detection, while its high inference efficiency and continual learning capability underscore its scalability and practicality for real-world deployment.

References

- [1] Paul Bergmann, Michael Fauser, David Sattlegger, and Carsten Steger. Mvtec ad—a comprehensive real-world dataset for unsupervised anomaly detection. In Proceedings of the IEEE/CVF conference on computer vision and pattern recognition, pages 9592–9600, 2019.
- [2] Zhe Li, Chong Wang, Mei Han, Yuan Xue, Wei Wei, Li-Jia Li, and Li Fei-Fei. Thoracic disease identification and localization with limited supervision. In Proceedings of the IEEE conference on computer vision and pattern recognition, pages 8290–8299, 2018.
- [3] Alex Costanzino, Pierluigi Zama Ramirez, Giuseppe Lisanti, and Luigi Di Stefano. Multi-modal industrial anomaly detection by crossmodal feature mapping. In Proceedings of the IEEE/CVF Conference on Computer Vision and Pattern Recognition, pages 17234–17243, 2024.
- [4] Wenqiao Li, Bozhong Zheng, Xiaohao Xu, Jinye Gan, Fading Lu, Xiang Li, Na Ni, Zheng Tian, Xiaonan Huang, Shenghua Gao, et al. Multi-sensor object anomaly detection: Unifying appearance, geometry, and internal properties. In Proceedings of the Computer Vision and Pattern Recognition Conference, pages 9984–9993, 2025.
- [5] Yue Wang, Jinlong Peng, Jiangning Zhang, Ran Yi, Yabiao Wang, and Chengjie Wang. Multimodal industrial anomaly detection via hybrid fusion. In Proceedings of the IEEE/CVF Conference on Computer Vision and Pattern Recognition, pages 8032–8041, 2023.
- [6] Zhiyuan You, Lei Cui, Yujun Shen, Kai Yang, Xin Lu, Yu Zheng, and Xinyi Le. A unified model for multi-class anomaly detection. Advances in Neural Information Processing Systems, 35:4571–4584, 2022.
- [7] Haoyang He, Yuhu Bai, Jiangning Zhang, Qingdong He, Hongxu Chen, Zhenye Gan, Chengjie Wang, Xiangtai Li, Guanzhong Tian, and Lei Xie. Mambaad: Exploring state space models for multi-class unsupervised anomaly detection. arXiv preprint arXiv:2404.06564, 2024.
- [8] Leon Weninger, Oliver Rippel, Simon Koppers, and Dorit Merhof. Segmentation of brain tumors and patient survival prediction: Methods for the brats 2018 challenge. In International MICCAI brainlesion workshop, pages 3–12. Springer, 2018.
- [9] Wei Luo, Yunkang Cao, Haiming Yao, Xiaotian Zhang, Jianan Lou, Yuqi Cheng, Weiming Shen, and Wenyong Yu. Exploring intrinsic normal prototypes within a single image for universal anomaly detection. In Proceedings of the Computer Vision and Pattern Recognition Conference, pages 9974–9983, 2025.
- [10] Xiaoqi Zhao, Youwei Pang, Wei Ji, Baicheng Sheng, Jiaming Zuo, Lihe Zhang, and Huchuan Lu. Spider: A unified framework for context-dependent concept segmentation. arXiv preprint arXiv:2405.01002, 2024.
- [11] Xinlong Wang, Xiaosong Zhang, Yue Cao, Wen Wang, Chunhua Shen, and Tiejun Huang. Seggpt: Segmenting everything in context. arXiv preprint arXiv:2304.03284, 2023.
- [12] Vaishnav Potlapalli, Syed Waqas Zamir, Salman H Khan, and Fahad Shahbaz Khan. Promptir: Prompting for all-in-one image restoration. Advances in Neural Information Processing Systems, 36:71275–71293, 2023.
- [13] Aixin Liu, Bei Feng, Bing Xue, Bingxuan Wang, Bochao Wu, Chengda Lu, Chenggang Zhao, Chengqi Deng, Chenyu Zhang, Chong Ruan, et al. Deepseek-v3 technical report. arXiv preprint arXiv:2412.19437, 2024.
- [14] Zhihao Gu, Jiangning Zhang, Liang Liu, Xu Chen, Jinlong Peng, Zhenye Gan, Guannan Jiang, Annan Shu, Yabiao Wang, and Lizhuang Ma. Rethinking reverse distillation for multi-modal anomaly detection. In Proceedings of the AAAI Conference on Artificial Intelligence, volume 38, pages 8445–8453, 2024.
- [15] Hanqiu Deng and Xingyu Li. Anomaly detection via reverse distillation from one-class embedding. In Proceedings of the IEEE/CVF Conference on Computer Vision and Pattern Recognition, pages 9737–9746, 2022.
- [16] Karsten Roth, Latha Pemula, Joaquin Zepeda, Bernhard Schölkopf, Thomas Brox, and Peter Gehler. Towards total recall in industrial anomaly detection. In Proceedings of the IEEE/CVF Conference on Computer Vision and Pattern Recognition, pages 14318–14328, 2022.

- [17] Md Ashif Mahmud Joy, Shamima Nasrin, Ayesha Siddiqua, and Dewan Md Farid. Vitad: Leveraging modified vision transformer for alzheimer’s disease multi-stage classification from brain mri scans. Brain Research, 1847:149302, 2025.
- [18] Robert A Jacobs, Michael I Jordan, Steven J Nowlan, and Geoffrey E Hinton. Adaptive mixtures of local experts. Neural computation, 3(1): 79–87, 1991.
- [19] Noam Shazeer, Azalia Mirhoseini, Krzysztof Maziarz, Andy Davis, Quoc V Le, Geoffrey Hinton, and Jeff Dean. Outrageously large neural networks: The sparsely-gated mixture-of-experts layer. In International Conference on Learning Representations (2016), 2016. URL <https://openreview.net/forum?id=B1ckMDqlg>.
- [20] Joan Puigcerver, Carlos Riquelme, Basil Mustafa, and Neil Houlsby. From sparse to soft mixtures of experts. arXiv preprint arXiv:2308.00951, 2023.
- [21] Damai Dai, Chengqi Deng, Chenggang Zhao, RX Xu, Huazuo Gao, Deli Chen, Jiashi Li, Wangding Zeng, Xingkai Yu, Yu Wu, et al. Deepseekmoe: Towards ultimate expert specialization in mixture-of-experts language models. arXiv preprint arXiv:2401.06066, 2024.
- [22] Carlos Riquelme, Joan Puigcerver, Basil Mustafa, Maxim Neumann, Rodolphe Jenatton, André Susano Pinto, Daniel Keysers, and Neil Houlsby. Scaling vision with sparse mixture of experts. Advances in Neural Information Processing Systems, 34:8583–8595, 2021.
- [23] Xiaolei Wang, Xiaoyang Wang, Huihui Bai, Eng Gee Lim, and Jimin Xiao. Cnc: Cross-modal normality constraint for unsupervised multi-class anomaly detection. In Proceedings of the AAAI Conference on Artificial Intelligence, volume 39, pages 7943–7951, 2025.
- [24] Shiyuan Meng, Wenchao Meng, Qihang Zhou, Shizhong Li, Weiye Hou, and Shibo He. Moead: A parameter-efficient model for multi-class anomaly detection. In European Conference on Computer Vision, pages 345–361. Springer, 2024.
- [25] Zhikang Liu, Yiming Zhou, Yuansheng Xu, and Zilei Wang. Simplenet: A simple network for image anomaly detection and localization. In Proceedings of the IEEE/CVF Conference on Computer Vision and Pattern Recognition, pages 20402–20411, 2023.
- [26] Yunkang Cao, Jiangning Zhang, Luca Frittoli, Yuqi Cheng, Weiming Shen, and Giacomo Boracchi. Adaclip: Adapting clip with hybrid learnable prompts for zero-shot anomaly detection. In European Conference on Computer Vision, pages 55–72. Springer, 2024.
- [27] Chaoqin Huang, Aofan Jiang, Jinghao Feng, Ya Zhang, Xinchao Wang, and Yanfeng Wang. Adapting visual-language models for generalizable anomaly detection in medical images. In Proceedings of the IEEE/CVF Conference on Computer Vision and Pattern Recognition, pages 11375–11385, 2024.
- [28] Wenxin Ma, Xu Zhang, Qingsong Yao, Fenghe Tang, Chenxu Wu, Yingtai Li, Rui Yan, Zihang Jiang, and S Kevin Zhou. Aa-clip: Enhancing zero-shot anomaly detection via anomaly-aware clip. In Proceedings of the Computer Vision and Pattern Recognition Conference, pages 4744–4754, 2025.
- [29] Tsung-Yi Lin, Priya Goyal, Ross Girshick, Kaiming He, and Piotr Dollár. Focal loss for dense object detection. In Proceedings of the IEEE international conference on computer vision, pages 2980–2988, 2017.
- [30] Yu Tian, Guansong Pang, Fengbei Liu, Yuanhong Chen, Seon Ho Shin, Johan W Verjans, Rajvinder Singh, and Gustavo Carneiro. Constrained contrastive distribution learning for unsupervised anomaly detection and localisation in medical images. In Medical Image Computing and Computer Assisted Intervention–MICCAI 2021: 24th International Conference, Strasbourg, France, September 27–October 1, 2021, Proceedings, Part V 24, pages 128–140. Springer, 2021.
- [31] Junjie Hu, Yuanyuan Chen, and Zhang Yi. Automated segmentation of macular edema in oct using deep neural networks. Medical image analysis, 55:216–227, 2019.
- [32] Jinan Bao, Hanshi Sun, Hanqiu Deng, Yinsheng He, Zhaoxiang Zhang, and Xingyu Li. Bmad: Benchmarks for medical anomaly detection. In Proceedings of the IEEE/CVF Conference on Computer Vision and Pattern Recognition, pages 4042–4053, 2024.

- [33] Thomas Defard, Aleksandr Setkov, Angelique Loesch, and Romaric Audigier. Padim: a patch distribution modeling framework for anomaly detection and localization. In International Conference on Pattern Recognition, pages 475–489. Springer, 2021.
- [34] Haoyang He, Jiangning Zhang, Hongxu Chen, Xuhai Chen, Zhishan Li, Xu Chen, Yabiao Wang, Chengjie Wang, and Lei Xie. Diad: A diffusion-based framework for multi-class anomaly detection. arXiv preprint arXiv:2312.06607, 2023.
- [35] Jongheon Jeong, Yang Zou, Taewan Kim, Dongqing Zhang, Avinash Ravichandran, and Onkar Dabeer. Winclip: Zero-/few-shot anomaly classification and segmentation. In Proceedings of the IEEE/CVF Conference on Computer Vision and Pattern Recognition, pages 19606–19616, 2023.
- [36] Sergey Zagoruyko and Nikos Komodakis. Wide residual networks. In Proceedings of the British Machine Vision Conference 2016. British Machine Vision Association, 2016.
- [37] Brats 2020: Brain tumor segmentation challenge. <https://www.med.upenn.edu/cbica/brats2020/data.html>, 2020.
- [38] Lei Fan, Junjie Huang, Donglin Di, Anyang Su, Tianyou Song, Maurice Pagnucco, and Yang Song. Salvaging the overlooked: Leveraging class-aware contrastive learning for multi-class anomaly detection. In Proceedings of the IEEE/CVF International Conference on Computer Vision, pages 21419–21428, 2025.
- [39] Dmitry Lepikhin, HyoukJoong Lee, Yuanzhong Xu, Dehao Chen, Orhan Firat, Yanping Huang, Maxim Krikun, Noam Shazeer, and Zhifeng Chen. Gshard: Scaling giant models with conditional computation and automatic sharding. arXiv preprint arXiv:2006.16668, 2020.
- [40] William Fedus, Barret Zoph, and Noam Shazeer. Switch transformers: Scaling to trillion parameter models with simple and efficient sparsity. Journal of Machine Learning Research, 23(120): 1–39, 2022.
- [41] Paul Bergmann, Xin Jin, David Sattlegger, and Carsten Steger. The mvtec 3d-ad dataset for unsupervised 3d anomaly detection and localization. arXiv preprint arXiv:2112.09045, 2021.
- [42] Luca Bonfiglioli, Marco Toschi, Davide Silvestri, Nicola Fioraio, and Daniele De Gregorio. The eyecandies dataset for unsupervised multimodal anomaly detection and localization. In Proceedings of the Asian Conference on Computer Vision, pages 3586–3602, 2022.
- [43] Yang Zou, Jongheon Jeong, Latha Pemula, Dongqing Zhang, and Onkar Dabeer. Spot-the-difference self-supervised pre-training for anomaly detection and segmentation. In European Conference on Computer Vision, pages 392–408. Springer, 2022.

use a resolution of 252×252 . We also evaluate recent generalist models, including AdaCLIP, MVFA, and AA-CLIP, which predict results for each modality separately and aggregate the outputs.

E More Quantitative Comparison

In this section, we compare additional metrics and comparison methods. As shown in Tab. 7, we compare with the latest method, CCL [38], using the same WideResNet50 backbone, and our approach achieves overall superior results.

F Ablation on Number of Activated Experts

We conduct an ablation study on the number of activated routed experts. As shown in Fig. 9, as the number of activated experts increases, the model’s image and pixel-level metrics show a slight improvement. However, each additional expert also increases the number of dynamic filtering operations, reducing inference efficiency. To balance inference efficiency and performance, we set the number of activated experts to 2. This is a commonly used activation number, adopted by many MoE-based methods [39, 40].

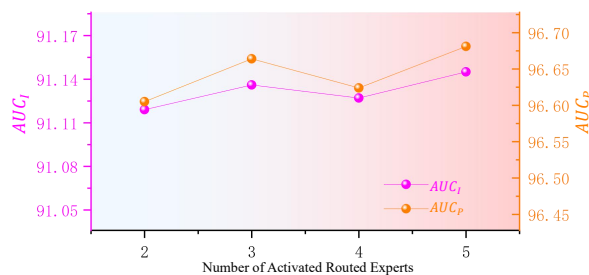


Figure 9. Impact of the number of activated routed experts on performance.

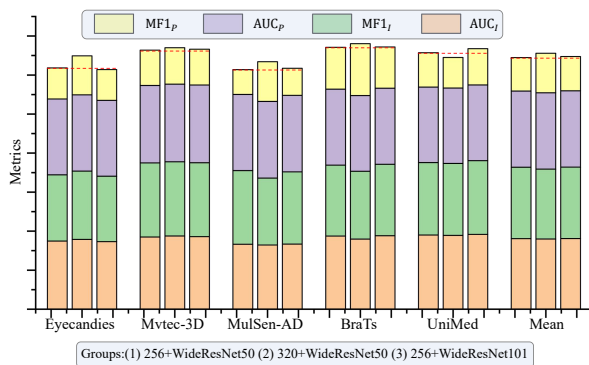


Figure 10. Impact of input resolution and backbone. Each group is divided into three settings: (1) 256×256 resolution + WideResNet50, (2) 320×320 resolution + WideResNet50, and (3) 256×256 resolution + WideResNet101.

G Influence of Resolution and Backbone

As shown in Fig. 10, we conducted an ablation study to assess the impact of input resolution and backbone architecture on model performance. Overall, larger image sizes and more powerful pre-trained models resulted in improved performance, demonstrating the scalability of our model in these aspects. This highlights the model’s scalability in both input resolution and backbone architecture. Specifically, larger image sizes result in more significant improvements for the RGB-D datasets Eyecandies and MVtec-3D, likely due to the correlation with anomaly size and point cloud accuracy. Higher resolutions help the model capture finer defect localization. Larger backbones improve anomaly localization for medical lesions, likely due to the enhanced generalization ability of larger models in medical image tasks.

H Per-Class Results

This section presents a class-wise comparison between the proposed method and recent state-of-the-art baselines. Tabs. 10–13 illustrate that our method outperforms mainstream multi-class approaches on the widely used datasets MVtec-AD and VisA. Tab. 14 and Tab.15 summarize image-level and pixel-level results on MVtec-3D [41]. The proposed approach attains the best scores on categories dominated by geometric defects (e.g., Potato) and on anomalies that benefit from multi-modal cues (e.g., Carrot). On the synthetic Eyecandies benchmark (Tabs. 16–17), our model achieves high accuracy on the ChocolateCookie and Peppermint-Candy classes. These results indicate that the method effectively exploits complementary RGB–Depth information to pinpoint fine-grained anomalies. Tab. 19 and 20 report infrared-based results on MulSen-AD, highlighting the model’s strength in detecting subsurface defects. In addition, Tab. 18 and 9 list results on UniMed and BraTS 2020 datasets, showing that the unified model remains competitive despite large domain shifts. Overall, the class-wise analysis confirms that our unified framework generalizes across modalities and defect types, consistently outperforming prior work.

I More Qualitative Comparison

Fig. 11, Fig. 13, Fig. 14, and Fig. 12 show more qualitative comparison on MVtec-3D (industrial RGB-D), Eyecandies (synthetic RGB-D), BraTs2020 (Brain Tumor), UniMed (three medical datasets) and MulSen-AD (industrial infrared). It demonstrates proposed method

Table 7. More comprehensive comparison on the MVTec-AD and VisA datasets under the super-multi-class setting with a resolution of 256×256 , evaluated using image-level metrics ($AUC_I/AP_I/MF1_I$) and pixel-level metrics ($AUC_P/MF1_P/AUPRO$).

Datasets	Publication	MVTec-AD		VisA	
Method↓	-	Image-level	Pixel-level	Image-level	Pixel-level
RD [15]	CVPR2022	95.8/97.8/95.0	95.1/51.5/90.7	88.4/89.9/86.7	96.8/38.7/87.0
UniAD [6]	NeurIPS2022	95.0/97.7/94.5	95.8/46.8/90.0	90.7/92.2/86.9	98.3/38.1/88.8
ViTAD [17]	CVIU2025	97.7/98.9/96.5	97.1/57.0/90.9	89.1/90.4/85.4	98.0/39.8/84.2
MambaAD [7]	NeurIPS2024	94.7/97.7/94.5	96.3/51.5/90.5	90.2/91.4/87.5	97.7/39.4/87.9
INP-Former [9]	CVPR2025	99.2/99.5/98.6	98.2/60.7/93.8	95.2/95.7/91.9	98.8/44.4/ 91.5
CCL [38]	ICCV2025	98.2/99.2/97.0	97.3/57.1/92.6	93.6/94.3/90.3	98.4/45.4/91.1
UniMMAD	Ours	99.4/99.6/98.7	98.1/60.2/93.0	95.5/96.2/92.4	98.9/47.2/91.3

Table 8. Overview of the Datasets.

Datasets	Fields	Modality	#Classes	Train		Test		
				#Items	#Images	#Items	#Images	
MVTec-3D [41]	Industrial	RGB, Depth	10	2656	5312	1197	2394	
Eyecandies [42]	Synthetic	Syn_RGB, Syn_Depth	10	8751	17502	500	1000	
MulSen-AD [4]	Industrial	Infrared	15	1391	1391	644	644	
MVTec-AD [1]	Industrial	RGB	15	3629	3629	2180	2180	
VisA [43]	Industrial	RGB	12	8659	8659	2162	2162	
Brats2020 [37]	Medical	Flair, T1, T2, T1CE	1	1183	4732	167	668	
UniMed	Hyper-Kvasir [30]	Medical	Endoscopy	1	2020	2020	184	184
	Retinal OCT [31]	Medical	OCT	1	1009	1009	270	270
	Liver CT [32]	Medical	CT	1	404	404	158	158

Table 9. Per-Class comparison on the BraTs2020 [37] Dataset.

Methods	Publication	AUC_I (%)	AP_I (%)	$MF1_I$ (%)	AUC_P (%)	$MF1_P$ (%)	AUPRO (%)
Specialized Models (One model for one dataset)							
PatchCore [16]+MMRD [14]	-	91.8	95.7	90.5	95.7	46.7	82.6
Generalist Models (One model performs all AD tasks without fine-tuning)							
AdaCLIP [26]	ECCV'24	70.7	81.7	81.6	96.6	48.4	78.2
MVFA [27]	CVPR'24	63.7	78.7	79.9	94.3	33.4	67.5
AA-CLIP [28]	CVPR'25	57.6	69.0	80.2	95.0	30.0	77.2
Unified Multi-modal and Multi-class Model							
UniMMAD	Ours	95.8	98.0	91.1	97.5	51.4	84.4

Table 10. Per-Class comparison on the MVTec-AD [1] Dataset for image-level metrics: $AUC_I/AP_I / MF1_I$.

Method→ Class↓	RD [15] CVPR'22	UniAD [6] NeurIPS'22	ViTAD [17] CVIU'25	MambaAD [7] NeurIPS'24	INP-Former [9] CVPR'25	UniMMAD Ours
Capsule	91.4/98.0/93.9	85.8/96.6/91.9	94.0/98.6/95.4	84.7/96.2/93.3	97.4/98.2/96.7	97.6/99.3/97.2
Carpet	97.9/99.4/96.0	99.9/99.9/99.4	99.4/99.8/99.4	96.7/99.0/95.4	100./100./100.	99.3/99.7/98.3
Grid	92.3/97.2/93.2	97.2/99.1/96.4	99.3/99.7/99.1	96.8/99.0/97.2	100./100./100.	100./99.7/100.
Leather	100./100./100.	100./100./100.	100./100./100.	100./100./100.	100./100./100.	100./99.8/100.
Tile	98.5/99.4/96.4	99.1/99.6/97.0	100./100./100.	99.4/99.7/97.6	100./100./100.	100./99.8/100.
Wood	99.2/99.7/ 98.3	98.2/99.4/97.5	98.6/99.5/96.7	99.5/99.8/98.3	99.2/99.1/98.1	98.8/99.4/97.6
Bottle	99.7/99.9/98.4	99.9/99.9/99.2	100./100./100.	99.4/99.8/98.4	100./100./100.	100./99.8/100.
Cable	78.9/86.8/80.5	84.5/91.9/81.2	97.3/98.4/93.3	85.4/91.2/83.7	99.5/ 99.9/98.4	99.6/99.5/97.3
Hazelnut	99.8/99.9/98.5	99.9/99.9/99.2	99.1/99.5/96.4	99.9/99.9/99.2	100./100./100.	100./99.7/100.
Metal nut	99.1/99.7/97.3	99.3/99.8/97.8	99.3/99.8/98.4	97.5/99.4/95.7	100./100./100.	100./99.8/100.
Pill	95.7/99.2/95.7	94.4/98.9/94.5	96.9/99.4/96.1	88.2/97.6/93.1	98.3/99.1/96.8	97.9/ 99.6/97.1
Screw	96.1/98.7/94.9	83.1/93.0/88.0	87.1/95.5/88.2	89.0/96.0/90.1	95.0/98.2/94.0	98.2/99.4/97.0
Toothbrush	99.1/99.6/98.3	91.9/96.4/93.7	99.7/99.8/98.3	97.7/99.1/95.2	100./100./100.	99.4/99.3/98.3
Transistor	88.8/88.3/85.0	93.7/91.0/84.4	95.9/94.2/88.6	89.2/88.8/83.3	99.0/98.3/95.3	99.6/98.7/98.7
Zipper	99.3/99.8/98.7	97.6/99.3/97.1	97.6/99.2/97.5	96.5/98.9/96.7	100./100./100.	99.6/99.8/99.1
Mean	95.7/97.7/95.0	95.0/97.7/94.5	97.7/98.9/96.5	94.7/97.6/94.5	99.2/99.5/98.6	99.4/99.6/98.7

Table 11. Per-Class comparison on the MVTec-AD [1] dataset for pixel-level metrics: AUC_P / $MF1_P$ / AUPRO.

Method→ Class↓	RD [15] CVPR'22	UniAD [6] NeurIPS'22	ViTAD [17] CVIU'25	MambaAD [7] NeurIPS'24	INP-Former [9] CVPR'25	UniMMAD Ours
Capsule	98.5/47.5/95.0	98.5/48.3/92.5	97.9/47.9/92.2	98.6/44.4/94.3	99.0/52.1/95.6	98.9/50.2/92.5
Carpet	98.9/60.2/95.4	98.5/56.1/ 95.6	98.8/ 62.2 /94.2	98.5/56.4/93.8	99.1 /60.8/95.3	99.0/ 62.2 /95.1
Grid	98.8/43.3/ 96.1	96.2/28.4/90.8	98.4/36.5/95.3	98.8/46.8/96.0	98.4/40.4/94.6	99.0/47.2 /95.5
Leather	99.3/47.0/97.7	98.9/43.5/ 98.1	99.5/53.5 /97.9	99.1/43.7/97.6	99.2/42.9/96.1	99.4/52.8/97.4
Tile	94.4/57.1/84.0	92.4/51.6/81.1	96.4/ 68.1 /87.4	92.5/53.5/79.0	97.5 /67.5/ 91.0	96.0/63.7/89.0
Wood	95.2/50.6/91.0	92.8/43.1/89.6	95.9/56.0/87.6	94.3/44.7/89.6	96.4/59.5/91.3	94.9/50.7/88.0
Bottle	97.3/66.2/93.5	97.4/64.9/92.7	98.7/73.9/94.6	97.2/64.8/93.2	99.0/78.6/95.6	98.7/74.4/93.4
Cable	77.4/30.8/73.5	91.4/32.1/77.0	92.4/41.4/85.4	88.2/33.1/78.9	98.7/67.5/94.4	97.8/60.8/91.9
Hazelnut	98.5/59.1/ 95.6	97.9/56.0/94.6	98.7/61.3/94.7	98.5/59.3/95.3	99.2/68.7 /95.3	98.9/64.0/94.8
Metal nut	91.3/57.1/89.1	92.2/57.5/87.2	95.5/74.7/92.1	93.9/62.7/90.4	96.6/79.2/93.3	97.4/81.8/94.1
Pill	96.6/58.7/95.6	94.5/45.5/95.4	98.6/75.4 /95.6	97.4/64.0/95.4	97.2/65.1/ 96.5	98.1/69.3/95.5
Screw	99.0/41.0/95.8	98.6/33.9/93.7	98.6/38.7/92.6	99.0/44.4/95.7	99.4/46.9/96.0	99.4/45.7/96.0
Toothbrush	98.7/55.7/90.8	97.9/45.0/85.1	99.1/64.9 /90.9	98.8/57.6/89.6	99.0/58.8/ 93.5	99.1 /62.4/91.7
Transistor	83.4/39.5/71.0	92.1/45.4/82.8	92.0/51.4/74.0	90.3/41.5/73.4	96.0/61.9 /84.2	95.7/61.2/ 85.5
Zipper	98.2 /58.1/ 94.7	97.1/49.3/92.4	95.8/49.8/89.4	98.0/55.5/94.0	98.1/ 59.6 /94.2	97.8/55.5/93.2
Mean	95.0/51.5/90.6	95.8/46.7/89.9	97.1/57.0/90.9	96.2/51.5/90.4	98.2/60.6/93.8	98.1/60.2/93.0

can accurately segment defect and lesion for a wide range of classes. In RGB-D datasets such as Cookie, our heatmaps highlight elongated defects along fiber directions. The model also emphasizes depth-based holes (e.g., Peach) and RGB-based color contamination (e.g., Candy Cane). In medical datasets such as UniMed, our method effectively separates boundary-blurred lesions from normal tissues, enabling high-confidence localization of conditions like colon polyps and brain tumors. Some generalist models like MVFA and AdaCLIP also show confident segmentation for colon polyps, possibly due to overlaps with their supervised training data. However, they incorrectly focus on normal regions in MulSen-AD, Liver Tumor, and Macular Edema. In contrast, UniMMAD consistently delivers accurate defect localization across diverse scenes, modalities, and object categories. These results highlight the effectiveness of the proposed “general \rightarrow specific” paradigm and domain-specific reconstruction pathways in C-MoE, which mitigate cross-domain reconstruction interference. UniMMAD demonstrates precise defect localization and sharper boundaries.

Table 12. Per-Class comparison on the VisA [43] dataset for image-level metrics: $AUC_I/AP_I / MF1_I$.

Method→ Class↓	RD [15] CVPR'22	UniAD [6] NeurIPS'22	ViTAD [17] CVIU'25	MambaAD [7] NeurIPS'24	INP-Former [9] CVPR'25	UniMMAD Ours
Candle	89.0/89.3/82.2	93.8/94.4/86.2	87.3/88.2/82.1	90.3/91.2/84.2	97.4/97.2/92.6	95.3/94.8/90.3
Capsules	75.2/86.0/78.4	74.8/85.2/78.6	78.6/87.0/78.1	76.8/84.1/80.8	90.3/94.8/88.5	88.5/93.6/84.6
Cashew	87.8/93.6/88.1	91.1/95.6/88.6	82.2/91.1/86.0	88.5/94.2/88.1	95.5/97.6/ 93.9	95.7/98.0/93.2
Chewinggum	91.1/95.5/88.8	97.4/98.8/95.7	92.1/96.3/88.3	89.8/95.1/87.0	98.3/99.3/96.4	98.8/99.5/97.9
Fryum	94.7/97.6/90.8	92.3/96.3/91.2	93.3/97.0/89.6	94.8/97.8/92.0	98.0/99.0/94.8	96.2/98.3/92.8
Macaroni1	92.2/89.9/86.3	87.5/83.1/79.6	84.5/81.2/77.9	88.9/87.7/82.2	94.2/93.3/88.6	97.2/97.2/91.5
Macaroni2	80.7/76.6/75.7	76.2/76.0/69.2	78.3/71.8/73.9	69.6/60.9/71.0	82.5/79.8/78.5	83.3/82.4/79.4
Pcb1	95.1/94.9/91.0	96.5/96.0/92.7	95.3/93.7/90.4	96.1/95.9/90.6	97.3/96.7/95.1	97.1/96.5/95.0
Pcb2	97.4/97.6/93.1	92.4/92.8/86.2	90.8/89.4/85.7	95.6/96.1/90.9	96.7/96.3/91.5	97.2/97.1/ 94.0
Pcb3	60.0/58.9/70.4	88.4/88.6/81.2	90.8/91.4/83.5	94.5/94.6/88.8	95.1/95.7/87.8	97.1/97.3/93.0
Pcb4	99.9/99.9/99.0	99.4/99.4/96.4	98.9/98.7/96.1	99.7/99.7/97.5	99.7/99.8/97.5	99.8/99.6/98.0
Pipe fryum	97.3/98.6/95.5	97.9/99.1/96.0	95.9/98.0/92.8	97.7/98.7/96.5	97.3/98.8/97.5	99.8/99.7/99.0
Mean	88.4/89.9/86.6	90.6/92.1/86.8	89.0/90.3/85.4	90.2/91.3/87.5	95.2/95.7/91.9	95.5/96.2/92.4

Table 13. Per-Class comparison on the VisA [43] dataset for pixel-level metrics: $AUC_P/MF1_P / AUPRO$.

Method→ Class↓	RD [15] CVPR'22	UniAD [6] NeurIPS'22	ViTAD [17] CVIU'25	MambaAD [7] NeurIPS'24	INP-Former [9] CVPR'25	UniMMAD Ours
Candle	98.8/34.4/94.3	99.2/33.4/94.9	95.4/26.1/83.7	99.0/30.0/ 95.9	99.4/37.9/95.2	99.3/37.0/94.7
Capsules	99.0/56.2/90.9	97.4/40.6/77.6	98.1/41.9/74.7	98.4/46.2/88.0	99.4/56.5/91.4	99.6/65.8/91.9
Cashew	87.3/42.5/68.3	97.5/47.7/90.6	97.4/58.6/69.1	91.2/45.2/70.3	97.6/60.5/89.3	98.8/62.3/90.7
Chewinggum	97.3/52.7/68.8	99.3/61.9/87.3	97.2/57.3/68.8	96.6/52.9/62.0	98.6/58.8/82.9	98.4/59.9/81.9
Fryum	96.8/50.3/ 92.6	96.9/50.4/86.5	97.3/51.2/88.9	96.9/51.5/92.2	97.1/48.6/89.9	97.0/ 52.5/88.4
Macaroni1	99.7/32.2/96.4	99.1/15.4/93.8	98.3/15.3/89.6	99.5/26.4/95.9	98.8/21.1/91.9	99.3/ 32.8/92.4
Macaroni2	99.4/17.6/95.2	97.7/10.4/89.6	98.1/10.1/87.3	98.5/ 8.6/91.1	99.0/11.7/93.5	98.9/16.9/92.1
Pcb1	99.2/54.0/95.1	99.2/57.0/91.2	99.3/56.8/88.7	99.5/65.8/ 95.2	99.7/68.5/94.9	99.7/72.9/94.8
Pcb2	97.7/29.4/90.9	98.1/19.4/86.1	98.0/21.1/83.4	98.5/24.8/ 92.5	98.9/31.5/89.9	98.8/26.5/ 92.5
Pcb3	89.7/ 3.5/67.7	98.3/28.2/86.7	98.0/28.5/88.0	98.5/29.5/ 93.9	99.1/30.1/91.7	99.1/29.0/91.1
Pcb4	97.3/34.6/87.3	97.5/39.6/86.1	98.9/44.7/92.7	96.1/35.8/81.7	98.7/ 45.9/92.1	98.4/43.1/90.9
Pipe fryum	98.9/56.7/ 95.7	98.7/52.3/94.1	99.4/66.0/94.3	99.0/55.2/95.2	99.2/60.9/94.9	99.3/ 67.5/94.2
Mean	96.8/38.7/86.9	98.2/38.0/88.7	97.9/39.8/84.1	97.6/39.3/87.8	98.8/44.3/ 91.5	98.9/47.2/91.3

Table 14. Per-Class comparison on the MVTEC-3D [41] dataset for image-level metrics: $AUC_I/AP_I / MF1_I$.

Method→ Class↓	M3DM [5] CVPR'23	CFM [3] CVPR'24	AdaCLIP [26] ECCV'24	MVFA [27] CVPR'24	AACLIP [28] CVPR'25	UniMMAD Ours
Bagel	98.7/ 99.9/98.1	99.2/99.8/97.8	85.3/95.6/92.1	62.1/87.4/89.3	78.5/93.8/89.2	94.4/98.5/94.2
Cable gland	84.7/96.1/92.3	81.8/95.1/89.8	61.6/87.8/90.2	57.7/82.6/89.2	49.5/82.3/89.7	94.8/98.5/96.0
Carrot	94.6/99.0/95.6	97.8/99.5/97.3	80.4/95.8/91.7	71.3/92.5/91.8	64.5/89.5/91.9	99.4/99.8/98.8
Potato	95.8/99.4/96.2	88.4/96.8/93.3	63.3/86.7/90.2	48.4/80.1/89.3	87.5/96.7/92.1	93.3/97.9/ 96.2
Rope	91.6/96.8/89.1	93.8/97.5/90.9	82.5/90.9/85.5	91.6/96.6/91.5	81.3/91.8/84.1	97.5/99.0/97.1
Foam	91.4/98.0/94.3	91.4/97.8/92.0	69.5/91.2/88.9	53.6/86.9/88.9	49.7/81.8/88.9	89.1/97.3/91.6
Dowel	89.2/95.7/92.3	92.7/98.2/92.4	73.1/92.7/89.7	55.4/84.0/88.9	46.3/79.5/87.9	95.9/98.8/96.2
Tire	87.3/96.0/92.1	86.6/95.8/90.4	61.6/85.8/87.4	46.9/76.8/87.4	74.4/88.2/90.5	70.4/88.0/88.7
Peach	92.3/97.8/95.1	93.4/98.2/95.0	77.4/92.7/92.0	67.0/86.9/90.0	87.6/96.1/91.2	95.8/98.8/96.3
Cookie	95.6/98.9/96.1	98.9/99.7/ 98.5	86.4/95.5/91.8	73.7/89.9/88.4	99.1/99.8/98.5	94.2/98.3/93.4
Mean	92.1/97.7/94.1	92.4/ 97.8/93.7	74.1/91.4/89.9	62.7/86.3/89.4	71.8/89.9/90.4	92.5/97.5/94.9

Table 15. Per-Class comparison on the MVTec-3D [41] dataset for pixel-level metrics: AUC_P/MF1_P / AUPRO.

Method→ Class↓	M3DM [5] CVPR'23	CFM [3] CVPR'24	AdaCLIP [26] ECCV'24	MVFA [27] CVPR'24	AACLIP [28] CVPR'25	UniMMAD Ours
Bagel	99.4/51.4/96.4	99.3/ 52.8/96.9	98.6/49.4/92.0	88.2/ 6.0/50.4	99.0/44.3/94.1	98.8/48.0/94.2
Cable gland	99.3/47.5/97.0	98.0/28.2/93.1	96.1/30.6/85.6	91.7/ 4.0/72.9	96.1/29.6/86.7	99.2/44.6/ 97.1
Carrot	99.6/41.4/97.7	99.8/53.7/97.9	98.7/27.6/95.2	97.3/13.6/91.3	99.6/44.1/97.6	99.6/43.6/ 97.9
Potato	99.4/40.4/96.8	99.5/34.0/97.4	99.4/31.1/96.8	97.7/10.6/90.5	99.7/51.5/97.8	99.6/42.1/ 97.8
Rope	99.6/49.4/ 96.5	99.7/63.8/96.3	98.6/46.1/93.4	97.3/29.1/87.7	99.5/53.3/95.4	99.4/39.5/96.4
Foam	98.5/43.5/93.7	98.7/48.1/94.1	90.7/42.7/70.3	91.9/28.0/73.0	95.1/ 9.9/84.6	97.4/38.9/90.3
Dowel	96.8/33.7/91.1	97.6/35.0/91.6	94.3/10.2/83.1	89.8/ 7.5/72.6	98.4/ 37.1/93.2	98.9/35.1/96.0
Tire	99.3/41.2/96.3	98.9/17.1/95.1	97.2/40.7/87.6	93.1/ 7.8/76.8	98.9/26.7/95.9	98.6/36.8/94.6
Peach	99.5/42.4/97.4	99.2/43.0/96.4	98.3/31.1/93.3	95.1/ 8.8/81.6	97.6/ 59.6/94.7	99.5/48.7/97.5
Cookie	97.8/56.2/92.4	96.8/ 65.5/93.9	97.2/61.1/93.3	90.3/24.3/72.7	96.8/64.8/94.0	99.3/63.8/96.9
Mean	98.9/ 44.7/95.5	98.7/44.1/95.3	96.9/37.1/89.1	93.2/14.0/76.9	98.0/42.1/93.4	99.0/44.1/95.9

Table 16. Per-Class comparison on the Eyecandies [42] dataset for image-level metrics: AUC_I/AP_I / MF1_I.

Method→ Class↓	M3DM [5] CVPR'23	CFM [3] CVPR'24	AdaCLIP [26] ECCV'24	MVFA [27] CVPR'24	AACLIP [28] CVPR'25	UniMMAD Ours
Gummybear	75.2/81.3/73.2	79.3/ 84.7/77.3	58.2/62.2/66.7	55.0/50.4/66.7	52.2/55.5/67.6	90.7/84.3/89.7
Lollipop	78.7/61.7/69.0	80.7/ 76.6/71.0	70.0/52.6/59.1	63.6/43.8/56.2	42.5/26.5/49.2	85.1/76.1/78.7
Marshmallow	91.7/92.2/84.7	97.8/98.3/95.8	82.3/85.3/80.0	82.1/83.8/79.2	60.2/67.1/66.7	99.8/98.9/98.0
Licoricesandwich	79.8/80.1/80.0	88.6/91.8/84.3	63.4/58.9/69.3	69.0/65.3/69.6	47.5/49.4/67.6	90.0/92.6/86.9
Chocolatepraline	75.8/80.1/72.3	88.0/91.3/82.6	86.6/80.0/ 86.8	72.6/72.7/76.9	54.2/55.0/69.6	82.7/87.2/76.1
Chocolatecookie	74.4/70.6/74.1	88.2/90.9/83.7	78.7/85.3/76.2	58.1/61.6/69.3	55.8/55.6/66.7	97.9/98.1/96.0
Peppermintcandy	95.3/96.0/90.6	85.8/89.3/79.2	85.9/85.7/81.5	76.3/78.7/76.7	27.7/37.0/66.7	92.6/93.1/84.0
Hazelnuttruffle	53.4/55.8/66.7	71.7/80.1/69.6	37.6/40.3/66.7	60.0/57.7/ 70.0	42.6/42.4/67.6	61.9/64.6/69.6
Confetto	89.1/90.0/83.0	88.2/91.8/83.7	87.8/89.1/83.0	66.6/69.6/71.2	61.3/65.5/67.7	97.2/96.8/92.0
Candycane	60.3/62.2/66.7	49.6/47.5/68.6	80.6/77.0/79.3	44.8/50.7/66.7	37.8/43.4/66.7	57.4/57.2/69.5
Mean	77.3/77.0/76.0	81.8/84.2/79.6	73.1/71.6/74.8	64.8/63.4/70.2	48.1/49.7/65.6	85.5/84.9/84.1

Table 17. Per-Class comparison on Eyecandies [42] Dataset for pixel-level metrics: AUC_P/MF1_P / AUPRO.

Method→ Class↓	M3DM [5] CVPR'23	CFM [3] CVPR'24	AdaCLIP [26] ECCV'24	MVFA [27] CVPR'24	AACLIP [28] CVPR'25	UniMMAD Ours
Gummybear	94.8/37.4/78.5	93.1/19.3/78.9	96.6/25.2/87.6	88.6/ 4.7/53.7	88.3/ 6.6/64.8	95.9/ 41.5/88.6
Lollipop	96.5/28.6/77.5	98.3/22.2/93.0	97.7/11.4/87.8	95.1/ 6.1/78.4	97.3/13.6/88.9	98.0/ 30.2/90.3
Marshmallow	98.9/64.5/93.7	99.2/ 66.5/93.0	98.8/56.7/89.1	90.8/23.5/62.2	95.3/30.7/81.4	99.5/58.4/96.6
Licoricesandwich	96.8/ 43.4/85.4	96.0/28.1/81.7	95.6/31.5/80.3	82.8/11.2/47.6	95.6/36.4/81.4	98.4/39.4/93.5
Chocolatepraline	95.6/ 51.7/78.4	93.3/46.1/71.4	86.0/46.2/78.3	76.4/19.5/49.0	98.1/47.0/91.9	93.2/44.0/83.0
Chocolatecookie	89.4/23.5/71.4	97.5/35.5/86.9	95.8/ 46.3/86.8	50.0/12.8/19.5	94.3/45.1/84.0	98.5/43.5/93.1
Peppermintcandy	94.3/44.3/84.7	95.8/19.0/86.0	97.3/ 49.4/91.1	85.1/12.7/56.0	94.3/33.8/61.6	99.4/48.0/97.2
Hazelnuttruffle	89.2/19.0/61.0	90.8/38.2/61.6	87.6/ 7.1/53.5	71.6/ 4.3/42.1	87.8/ 5.6/ 96.2	90.6/23.4/65.2
Confetto	95.6/45.9/85.2	97.5/37.3/90.1	98.9/33.1/96.1	90.2/13.0/70.0	99.1/43.5/93.1	99.6/56.1/98.0
Candycane	85.7/ 6.4/70.8	97.2/ 6.6/90.6	98.0/13.1/93.3	95.7/ 2.7/87.3	97.5/ 9.3/70.8	95.4/ 9.4/86.9
Mean	93.7/36.5/78.7	95.8/31.9/83.3	95.1/32.0/84.4	82.6/11.1/56.6	94.7/27.2/81.4	96.9/39.4/89.2

Table 18. Per-Class comparison across UniMed datasets: Reinal OCT / Liver CT / Hyper-Kvasir / Mean performance.

Methods	AUC _I (%)	AP _I (%)	MF1 _I (%)	AUC _P (%)	AUPRO	MF1 _P (%)
Specialized Models (One model for one dataset)						
UniAD [6]	90.4/83.7/98.4/90.8	95.9/90.8/99.9/95.5	91.0/83.6/98.1/90.9	95.1/97.2/68.6/87.0	81.5/90.4/32.9/68.2	63.3/30.1/24.9/39.4
RD [15]	93.3/90.7/96.3/93.4	97.3/94.6/97.0/96.3	91.5/90.3/92.9/91.6	96.2/96.3/79.0/90.5	86.1/91.1/46.5/74.5	66.0/23.3/30.7/40.0
ViTAD [17]	95.3/92.9/98.3/95.5	98.1/95.5/98.7/97.4	93.8/92.6/94.4/93.6	94.5/97.4/83.5/91.8	80.3/93.4/52.6/75.4	63.4/35.1/34.9/44.4
MambaAD [7]	96.2/94.6/97.1/96.0	98.6/97.4/98.4/98.1	94.1/91.9/94.7/93.6	96.6/96.5/82.0/91.7	86.7/91.5/55.8/78.0	68.4/25.0/33.8/42.4
SimpleNet [25]	90.4/80.2/97.6/89.4	96.4/91.3/97.4/95.0	88.7/80.5/96.3/88.5	92.0/92.5/76.1/86.9	72.3/64.3/36.7/57.8	55.8/34.4/27.2/39.1
INP-Former [9]	97.4/91.0/99.8/96.1	99.0/95.5/99.1/97.9	94.9/90.1/98.1/94.4	95.2/97.2/85.6/92.7	81.6/90.3/57.5/76.5	67.2/33.2/36.0/45.5
Generalist Models (One model performs all AD tasks without fine-tuning)						
AdaCLIP [26]	82.4/70.8/98.2/83.8	92.6/82.2/98.8/91.2	85.1/84.8/95.9/88.6	91.2/92.2/88.8/90.7	78.2/87.7/67.5/77.8	51.9/18.0/58.7/42.9
MVFA [27]	88.6/89.2/88.5/88.8	94.7/95.1/91.7/93.8	91.0/87.3/83.3/87.2	89.2/96.3/77.1/87.5	65.3/87.5/54.7/69.2	43.2/22.4/37.3/34.3
AA-CLIP [28]	71.3/60.4/85.1/72.3	82.7/70.1/91.7/81.5	83.7/83.4/85.4/84.2	92.8/93.4/86.6/90.9	79.3/86.9/63.8/76.7	53.3/16.6/51.1/40.3
Unified Multi-scene, Multi-modal and Multi-class Model						
Ours	96.4/95.9/96.8/96.3	98.6/97.9/96.8/97.7	93.0/94.5/95.0/94.2	96.5/97.1/82.5/92.0	85.4/92.3/48.0/75.2	68.0/31.1/35.6/44.9

Table 19. Per-Class comparison on the MulSen-AD [4] dataset for image-level metrics: $AUC_I/AP_I / MF1_I$.

Method→ Class↓	MulSen-TripleAD [4] CVPR'25	AdaCLIP [26] ECCV'24	MVFA [27] CVPR'24	AA-CLIP [28] CVPR'25	UniMMAD Ours
Cotton	100./100./100.	47.3/81.1/87.6	54.3/83.5/87.6	47.3/81.1/87.6	99.7/99.6/98.7
Cube	100./100./100.	96.6/96.3/91.3	90.3/84.5/85.7	96.6/96.3/91.3	98.1/96.8/93.3
Zipper	99.1/99.6/97.2	69.8/88.5/82.3	100./100./100.	69.8/88.5/82.3	100./99.4/100.
Toothbrush	91.3/96.3/89.8	34.0/37.6/66.7	44.4/49.4/65.4	98.4/99.0/96.2	81.4/80.5/85.2
Spring pad	67.5/86.2/85.7	74.4/70.1/76.9	91.0/91.0/84.8	85.8/92.9/ 90.5	91.6/93.2/86.6
Piggy	99.7/99.9/98.4	57.9/75.1/82.3	53.0/72.8/84.3	98.3/99.3/98.3	97.9/98.7/94.9
Capsule	96.8/99.3/96.0	52.4/83.8/89.1	74.9/91.5/88.5	87.0/97.2/91.4	94.2/98.1/95.8
Light	61.1/85.0/ 89.2	38.0/51.7/74.0	49.7/54.3/75.0	45.2/79.9/87.8	80.1/86.8/88.8
Plastic cylinder	99.6/ 99.9/98.2	88.3/94.6/88.9	71.7/85.1/80.8	100./99.5/100.	99.3/99.1/97.9
Screen	20.0/60.5/ 86.5	48.6/57.6/73.0	60.0/55.6/78.6	15.3/ 61.3/86.4	45.3/60.7/79.8
Screw	92.9/97.3/96.8	56.2/49.3/53.8	65.9/51.0/62.2	100./99.6/100.	75.0/60.6/82.4
Flat pad	95.3/ 98.6/93.5	84.6/86.8/88.9	51.3/64.0/76.7	95.6/98.4/ 95.0	97.6/97.9/93.8
Nut	33.4/71.8/85.3	43.2/29.7/53.1	61.5/42.6/61.9	46.3/ 78.2/86.9	75.0/72.9/79.9
Button cell	80.0/93.4/87.5	37.2/52.7/75.8	64.3/73.2/79.4	95.0/98.3/95.2	75.2/87.1/83.9
Solar panel	46.2/81.2/88.6	57.7/86.7/88.6	54.1/85.5/88.6	86.7/96.1/94.1	71.0/91.8/91.9
Mean	78.8/ 91.2/92.8	59.1/69.4/78.1	65.7/72.2/79.9	77.8/91.0/92.2	85.4/88.2/90.2

Table 20. Per-Class comparison on the MulSen-AD [4] dataset for pixel-level metrics: $AUC_P/MF1_P / AUPRO$.

Method→ Class↓	MulSen-TripleAD [4] CVPR'25	AdaCLIP [26] ECCV'24	MVFA [27] CVPR'24	AA-CLIP [28] CVPR'25	UniMMAD Ours
Cotton	92.6/ 30.8/77.1	94.1/30.7/85.1	82.8/21.3/56.0	94.1/30.7/85.1	96.8/25.6/89.1
Cube	99.9/72.5/96.4	99.8/65.2/92.2	90.1/39.8/52.6	99.8/65.2/92.2	99.7/66.1/92.3
Zipper	99.1/43.0/96.4	99.1/46.6/96.6	77.0/25.1/52.0	99.1/46.6/96.6	98.8/36.3/95.8
Toothbrush	99.2/ 39.3/94.8	99.3/20.8/95.9	63.9/ 4.6/36.3	98.2/14.1/91.5	98.2/27.0/89.2
Spring pad	99.7/34.6/98.0	99.0/25.9/96.6	98.3/ 3.3/94.2	93.1/34.1/84.3	94.8/ 35.2/88.0
Piggy	97.0/29.4/90.4	95.8/22.1/85.3	92.1/10.0/69.7	98.1/32.5/87.4	98.5/33.8/91.0
Capsule	99.3/30.0/97.0	99.1/25.6/ 97.0	97.3/26.2/90.4	98.8/28.8/95.5	98.9/26.6/95.4
Light	96.7/16.9/91.7	97.3/20.0/93.9	95.8/ 25.2/76.8	97.2/19.5/92.7	98.5/25.0/94.7
Plastic cylinder	99.5/47.4/97.2	99.2/46.4/94.7	89.1/ 3.2/60.9	99.4/ 50.3/97.0	99.3/40.9/97.0
Screen	91.4/ 7.6/78.0	93.3/11.2/82.3	84.1/10.6/36.5	92.3/ 14.1/79.1	90.4/11.7/79.0
Screw	99.0/11.9/ 96.5	98.6/11.2/95.6	97.3/16.8/88.8	98.9/12.7/ 96.5	99.2/44.9/96.1
Flat pad	99.6/ 45.1/97.7	99.2/35.9/97.0	97.8/ 6.4/93.0	99.4/43.4/97.4	99.7/37.8/98.2
Nut	99.6/36.8/97.1	98.9/16.7/96.0	98.0/ 2.2/94.0	98.5/34.1/92.4	98.8/ 45.3/89.6
Button cell	99.7/38.9/98.0	99.7/40.8/98.2	99.6/28.1/98.2	99.5/41.6/97.9	99.7/42.7/98.3
Solar panel	95.1/19.7/85.4	95.7/ 25.6/75.1	91.0/13.8/66.8	96.5/19.8/87.9	96.9/20.5/88.3
Mean	97.8/33.6/ 92.8	97.8/29.7/92.1	90.3/15.8/71.1	97.5/32.5/91.6	97.9/34.6/92.1

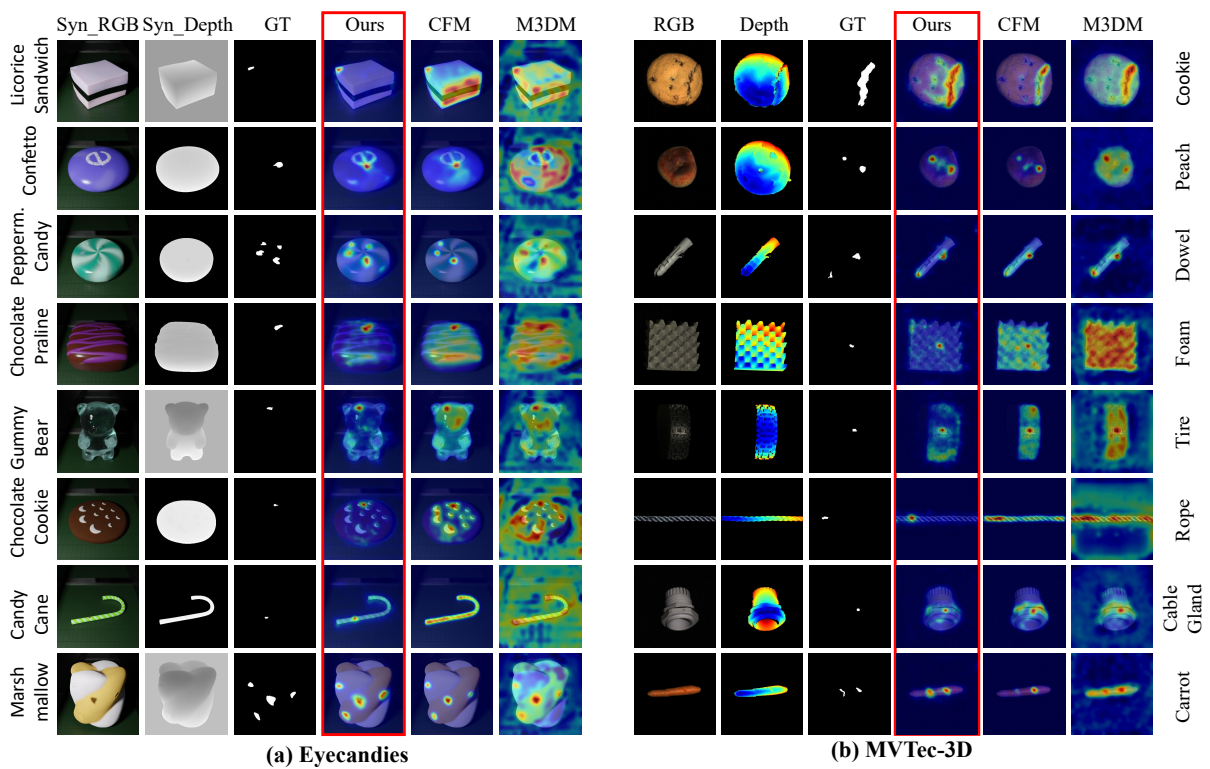


Figure 11. Qualitative comparison on MVTec-3D and Eyecandies, with our method highlighted in the red box.

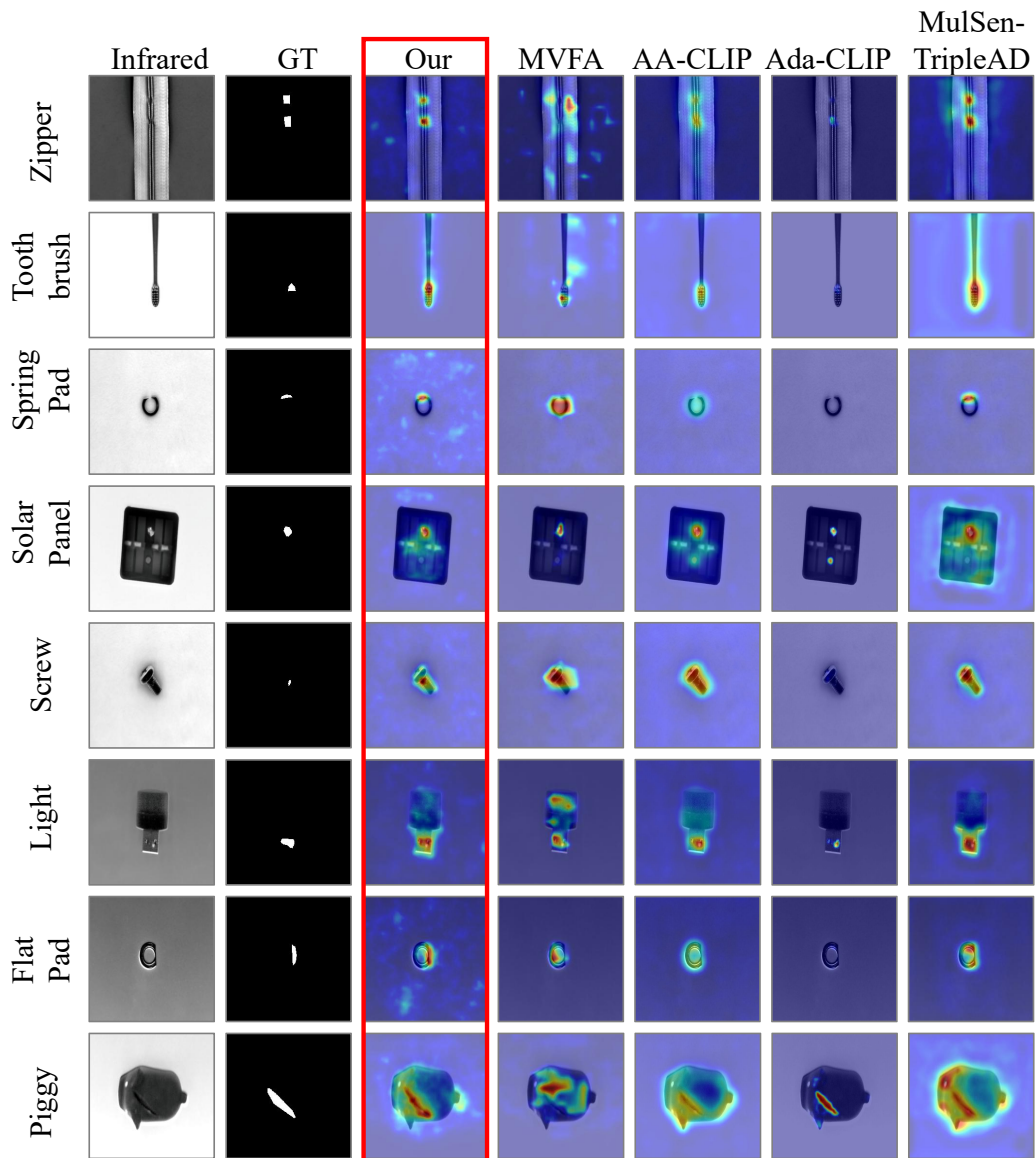


Figure 12. Qualitative comparison on MulSen-AD, with our method highlighted in the red box.

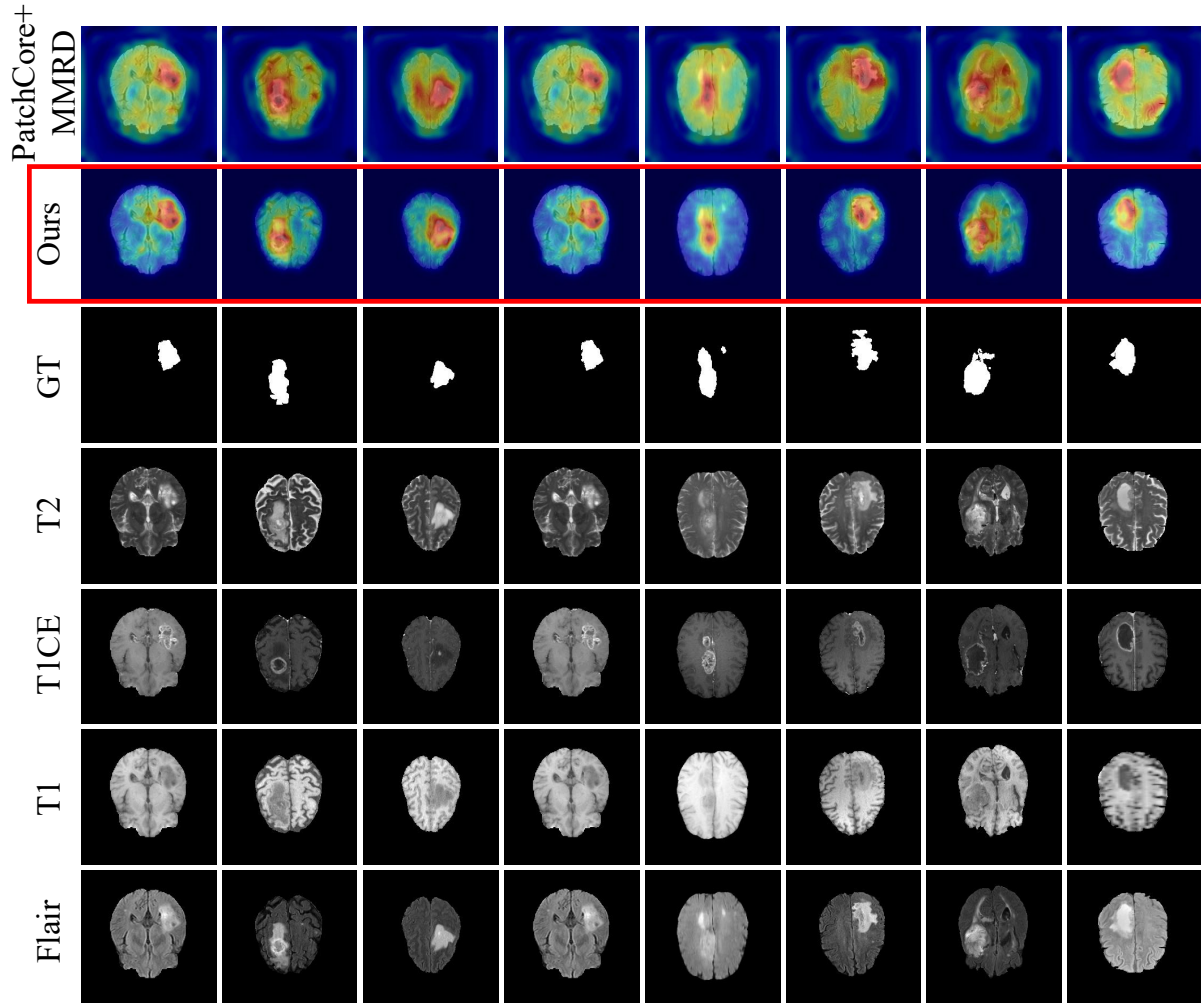


Figure 13. Qualitative comparison on BraTs2020, with our method highlighted in the red box.

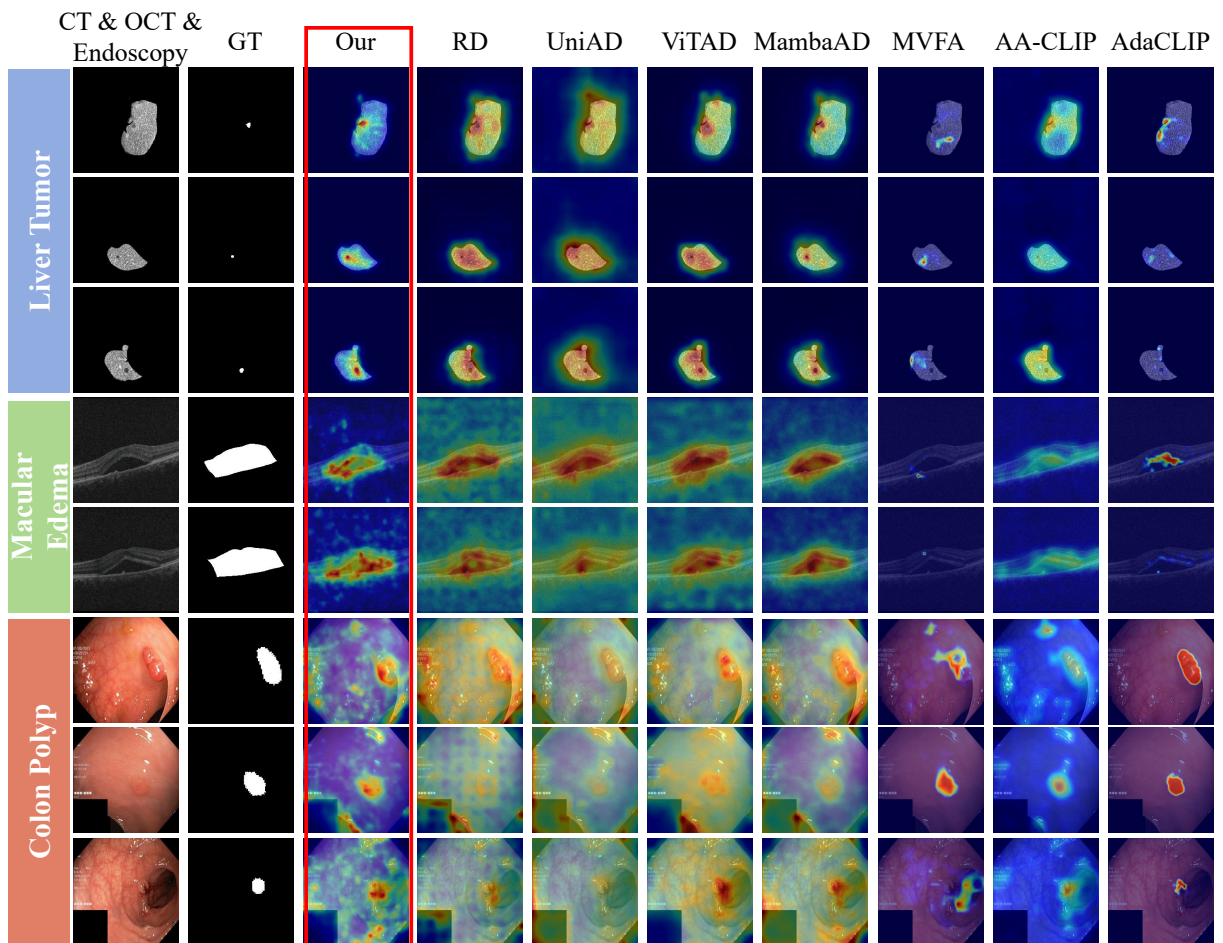


Figure 14. Qualitative comparison on UniMed, with our method highlighted in the red box.